doi:10.26443/seismica.v2i4.1678

Subducted Structure in Central Cascadia from Margin-Crossing Seismic Tomography

Sarah Nolan * [1,2], **Emilie E. E. Hooft** [3], **Asif Ashraf** [3], **Anne M. Tréhu** [1], **Douglas R. Toomey** [3], **Pieter-Ewald Share** [1], **Erin A. Wirth** [4], **Kevin M. Ward** [5]

[1]College of Earth, Ocean and Atmospheric Sciences, Oregon State University, Corvallis, OR, United States, [2]Department of Earth and Atmospheric Sciences, Cornell University, Ithaca, NY, United States, [3]Department of Earth Sciences, University of Oregon, Eugene, OR, United States, [4]United States Geological Survey, Seattle, WA, United States, [5]South Dakota School of Mines & Technology, Rapid City, SD, United States

Author contributions: *Conceptualization*: Anne Tréhu, Sarah Nolan, Emilie Hooft, Asif Ashraf. *Methodology*: Douglas Toomey, Emilie Hooft, Sarah Nolan, Asif Ashraf, Anne Tréhu. *Software*: Douglas Toomey, Emilie Hooft. *Validation*: Sarah Nolan. *Formal Analysis*: Sarah Nolan, Emilie Hooft, Asif Ashraf, Anne Tréhu. *Writing - Original draft*: Sarah Nolan, Emilie Hooft, Asif Ashraf. *Writing - Review & Editing*: Sarah Nolan, Emilie Hooft, Asif Ashraf, Anne Tréhu, Erin Wirth, Pieter-Ewald Share. *Visualization*: Sarah Nolan, Emilie Hooft, Asif Ashraf, Anne Tréhu. *Supervision*: Emilie Hooft, Anne Tréhu, Pieter-Ewald Share. *Funding acquisition*: Emilie Hooft, Anne Tréhu, Erin Wirth, Kevin Ward.

Abstract Studies indicate that the Cascadia Subduction Zone is capable of producing great earthquakes, and, like many other subduction zones, it exhibits along-strike differences in rupture history and plate coupling. Paleoseismic data, locking models, and microseismicity point to a change in seismic behavior around 44.5°N, offshore central Oregon. In this study, we use controlled-source seismic data from four shoreline-crossing experiments to invert for the P-wave velocity structure and Moho interface between 43.6°N and 45.2°N and to investigate changes in seismic structure within the forearc. The model reveals changes in the backstop geometry and an interpreted mafic dike embedded within an accreted terrane. WNW trending low-velocity anomalies along the Alvin Canyon Fault suggest the fault cuts through both the accretionary wedge and subducting oceanic plate. At the top of the subducting slab, nine circular high-velocity anomalies are present that we interpret to be seamounts at various stages of subduction. The final Moho interface shows significant changes in depth related to the density of accreted terranes within the overriding plate. We propose that the subducted topography is partially responsible for large slides and scars at the deformation front and that subducting seamounts may have uplifted broad regions along the margin. Evidence for ongoing deformation is provided by seismicity clustered near two of the proposed seamounts. Finally, we suggest that this rough plate interface may lead to lower coupling and/or have acted as a rupture barrier in past megathrust earthquakes.

Production Editor:
Alice Gabriel
Handling Editor:
Alice Gabriel
Copy & Layout Editor:
Miriam Gauntlett

Signed reviewer(s):
Dan Bassett, Suzanne Carbotte

Received:
2025-03-31
Accepted:
2025-07-28
Published:
2026-10-05

1 Introduction

Subduction zones exhibit along-strike variations in megathrust rupture history, plate coupling, and the distribution of microseismicity. In some regions, these segments persist through multiple earthquake cycles, providing valuable information about future ruptures. Subducting plate relief (Carbotte et al., 2024; Gase et al., 2021; von Huene et al., 2000; Martínez-Loriente et al., 2019), sediment thickness on the incoming plate (Bécel et al., 2017), slab geometry (Arnulf et al., 2022; Ashraf et al., 2025), and backstop architecture (Kopp, 2013) all contribute to the seismic behavior of a megathrust segment. A recent multi-margin study suggests that the interplay between multiple physical processes better explains changes in seismic behavior rather than a single factor (Bassett et al., 2025). Understanding the structure of the margin and its relationship to segmentation patterns is key.

A great Cascadia megathrust earthquake has never been recorded by geophysical instruments; however, paleoseismic studies show that this margin has produced numerous ruptures with heterogeneous slip distributions (Goldfinger et al., 2012; Walton et al., 2021). Measures of plate locking and observed seismicity suggest that Cascadia exhibits significant segmentation in seismic and aseismic behavior (Wech, 2021; Brudzinski and Allen, 2007). Megathrust segment boundaries have been identified at 46°N and 43°N based on the paleoseismic record, episodic tremor and slip (ETS), and geodetic locking models (Leonard et al., 2010; Goldfinger et al., 2012; Wang et al., 2013; Brudzinski and Allen, 2007; Schmalzle et al., 2014; Watt and Brothers, 2020). In Cascadia, these segmentation patterns have been attributed to changes in forearc structure (Watt and Brothers, 2020; Delph et al., 2021; Ashraf et al., 2025) or, alternatively, to changes in subslab buoyancy (Bodmer et al., 2018). Recently, Tréhu et al. (2023) and Carbotte et al. (2024) presented seismic imaging data indicating the presence of structures in the upper and lower plates, as well as deformation of the subducting plate that may contribute to a segment boundary around 44.5°N.

In this study, we seek to better understand the link between forearc structure and seismic behavior along the central Cascadia margin, which is characterized by

*Corresponding author: sn664@cornell.edu

low coupling and increased levels of microseismicity. We integrate data from over three decades of amphibious controlled-source seismic experiments, expanding the boundaries of the 3D volume imaged by Tréhu et al. (2023) to more comprehensively image the central Oregon forearc between 43.6°N and 45.2°N. Our high-resolution 3D P-wave velocity model and subducting plate Moho interface allow us to examine features of the forearc that are thought to control seismic behavior, including backstop geometry, Moho depth, and subducting plate topography.

1.1 Background

1.1.1 Tectonic Setting

The Cascadia Subduction Zone (CSZ) spans from northern California to Vancouver Island, where the Juan de Fuca plate subducts beneath continental North America. Paleoseismic studies suggest the last-known megathrust rupture of this margin occurred on January 26, 1700 (Satake et al., 2003). Geophysical modeling by Melgar (2021) suggests that the January 26, 1700 megathrust rupture had a minimum magnitude of $M \geq 8.7$ but the existence of additional partial margin ruptures around this time cannot be ruled out. The margin also exhibits down-dip and along-strike changes in plate coupling inferred from GNSS measurements shown in Figure 1B. Locking models quantify the extent to which the upper plate is coupled to the subducting plate and can help inform which regions are likely to exhibit large slip during future megathrust ruptures. Although the extent of locking at the trench is unresolved due to a lack of offshore instrumentation, multiple models show a significant decrease in locking within our study area (Schmalzle et al., 2014; Li et al., 2018; Lindsey et al., 2021).

In this study, we focus on the central Oregon segment of the margin, where the subducting Juan de Fuca plate is ~9 Ma old at the onset of subduction (Wilson, 2002) and is subducting obliquely at ~3.4 cm/yr (DeMets et al., 2010). The continental crust in central Cascadia is composed primarily of the thickened basaltic Siletz terrane. Siletzia is an oceanic plateau that was accreted to Oregon between 51-49 Ma (Wells et al., 2014) and extends from beneath the continental shelf to the western Cascades (Tréhu et al., 1994). A 2D seismic transect showed that the thickness of the Siletz terrane in the forearc of central Oregon increases from ~10 km offshore to ~30 km beneath the coastal range (Tréhu et al., 1994). Watt and Brothers (2020) refer to this as the static backstop and suggest that within this region, the western edge of Siletzia dips seaward at ~70°-90°. Magnetotelluric images show the Siletz terrane is resistive, suggesting the terrane is composed of low permeability rock (Egbert et al., 2022). A narrow portion of the sedimentary Franciscan terrane is thought to lie seaward of the Siletz terrane south of 44.7°N (Watt and Brothers, 2020; Carbotte et al., 2024; Ashraf et al., 2025) as seen in Figure 2A. The Franciscan terrane consists of pre-Tertiary to early Eocene rocks derived from accretionary wedge sediments and oceanic crust, which were later transported north to their current position (Carbotte et al., 2024; McLaughlin et al., 1997).

The distribution of recorded seismicity varies profoundly along the Cascadia margin (Figure 1A; Figure 2A) and at present, the CSZ lacks the moderate and large earthquakes that many other subduction zones regularly host on the megathrust. Earthquakes with M>3 are absent from the CSZ north of Cape Blanco except from 44.0°N to 45.0°N (Wang and Tréhu, 2016). This region has experienced frequent earthquakes, including two moderate-sized, low-angle thrust earthquakes (Mw 4.7 and Mw 4.9) in the summer of 2004 (Tréhu et al., 2008). Williams et al. (2011), Morton et al. (2023), Tréhu et al. (2015) and Stone et al. (2018) relocated smaller events in this region of the forearc and their catalogs reveal two earthquake clusters located near each of the moderate-sized 2004 earthquakes. The catalogs place most of these events at or above the plate interface. The northern earthquake cluster is located at 44.6°N and 124.4°W, coinciding with a free-air gravity low labeled G2 in Figure 2 , which Tréhu et al. (2012) identified. The southern cluster is located at 44.3°N and 124.4°W and includes a swarm of four nearly identical earthquakes with Mw 2.8-3.4 that occurred on January 25, 2013. Both clusters of earthquakes are thought to be caused by the interaction of two subducting seamounts with the overriding plate (Tréhu et al., 2012, 2015).

1.1.2 Previous Studies

Central Cascadia has been the target of multiple geophysical surveys over the last four decades, revealing several unique features. For instance, oblique subduction has resulted in the formation of a series of WNW strike-slip faults, including three offshore central Oregon (Goldfinger et al., 1997). As shown in Figure 2B, the Wecoma, Daisy Bank, and Alvin Canyon Faults all extend from the incoming plate seaward of the deformation front to approximately the seaward edge of Siletzia (SES). Recent high-resolution multi-channel seismic (MCS) data indicate that the Alvin Canyon Fault (ACF) bisects the upper and lower plates, potentially representing a tear in the slab (Carbotte et al., 2024). At the southern end of the ACF, a large mafic dike with similar WNW orientation is embedded within the Siletz terrane backstop and extends to the Yachats Basalt onshore (Tréhu et al., 2023). Tomography suggests this dike deflects the Moho beneath it by 2 to 4 km (Tréhu et al., 2023).

Active-source seismic studies (Kenyon, 2016), potential field models (Fleming and Tréhu, 1999), bathymetric data, and the relocation of microseismicity (Morton et al., 2018; Williams et al., 2011; Stone et al., 2018) suggest that there are several subducted seamounts located within the central Oregon forearc. Figure 2C shows the locations of two pronounced free-air gravity anomalies and four magnetic anomalies, respectively. The existence of a subducting seamount was proposed based on a gravity high (Fleming and Tréhu, 1999) beneath Hecata Bank. A second proposed seamount corresponds to a gravity low, G2, and a persistent cluster of seismicity. This seamount is thought to have sheared off from the subducting plate and caused the upper plate to erode, forming a basin (Tréhu et al., 2012). Further-

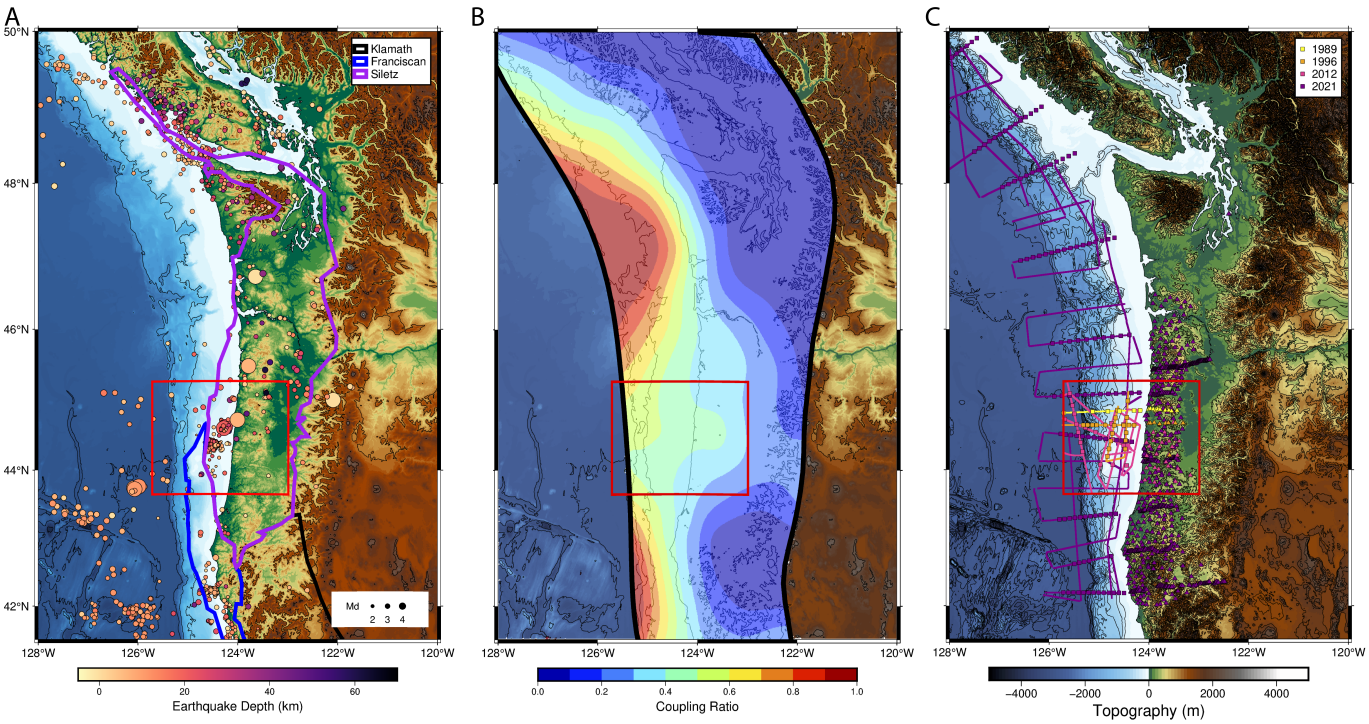


Figure 1 Maps of the Cascadia Subduction Zone (CSZ) with topography from the Global Multi-Resolution Topography Synthesis (Ryan et al., 2009). The red box outlines the bounds of our tomographic model. (A) Map showing the distribution of seismicity scaled by earthquake magnitude and colored by depth (Morton et al., 2023). Colored lines show the extent of the Siletz (purple), Franciscan (blue) and Klamath (black) terranes from Watt and Brothers (2020). (B) Coupling ratio from Lindsey et al. (2021). (C) Map shows the location of airgun shot lines, onshore seismometers (triangles), and ocean bottom seismometers and hydrophones (squares) from the four experiments used in this study. Shot lines and stations are colored based on the experiment year.

more, four magnetic anomalies labeled M1-M4 in Figure 2D are proposed to be associated with additional seamounts (Tréhu et al., 2012). Recently, CASIE21-MCS data revealed five subducting seamounts in this region (Figure 2B), including a seamount located slightly west of gravity high G1, and four others that do not appear to correlate with identified potential field anomalies (Carbotte et al., 2024).

Previous seismic imaging studies in the CSZ used local earthquakes (Dunham and Kiser, 2020), teleseisms (Delph et al., 2021; Bodmer et al., 2020), and ambient noise (Wang et al., 2019) to image large-scale features within the CSZ. Higher resolution, active-source seismic studies exist within this region but have largely been limited to 2D coverage (Tréhu et al., 1994; Gerdom et al., 2000; Han et al., 2016; Horning et al., 2016; Canales et al., 2017; Carbotte et al., 2022, 2024; Canales et al., 2023), with one 3D model covering a portion of this region (Kenyon, 2016; Kenyon et al., 2013; Tréhu et al., 2023), and a recent plate interface model spanning the offshore region (Carbotte et al., 2024). In this study, we add more than 388,000 new travel-time picks from the 2012 (Canales et al., 2017; Horning et al., 2016) and 2021 experiments (Canales et al., 2017; Carbotte et al., 2022; Tréhu et al., 2022a) to the existing set of travel time picks modeled by Tréhu et al. (2023). The expanded dataset is used to generate a high-resolution 3D image of the central Oregon margin, spanning the portion of the megathrust fault thought to be seismogenic. We compare our model to the observed patterns of along-strike changes in seismic and aseismic behavior.

2 Data

We used data from four controlled-source shore-crossing seismic studies spanning from 1989 to 2021 to develop a high-resolution 3D P-wave velocity model of the central Oregon forearc. Utilizing data from multiple studies, including newly collected data from the Cascadia2021 (Tréhu et al., 2022a) and CASIE21 (Canales et al., 2023) experiments, significantly expands our ray coverage and helps fill an important data gap. We used travel time picks for crustal turning waves in oceanic and continental crust (Pg), turning waves bottoming in the upper mantle of the subducting plate (Pn), and reflections from the subducting plate Moho (PmP). The number of arrivals modeled from each experiment year is shown in Supplementary Table S1 along with average uncertainties.

2.1 1989 and 1996 Data

The first onshore-offshore seismic survey to image this region of the Cascadia margin occurred in 1989. The study consisted of 6 ocean bottom seismometers (OBS) and hydrophones (OBH) and 10 land stations deployed along a line located at ~44.8°N. These instruments recorded airgun shots from a 64-gun commercial tuned array along a single transect, producing the first 2D

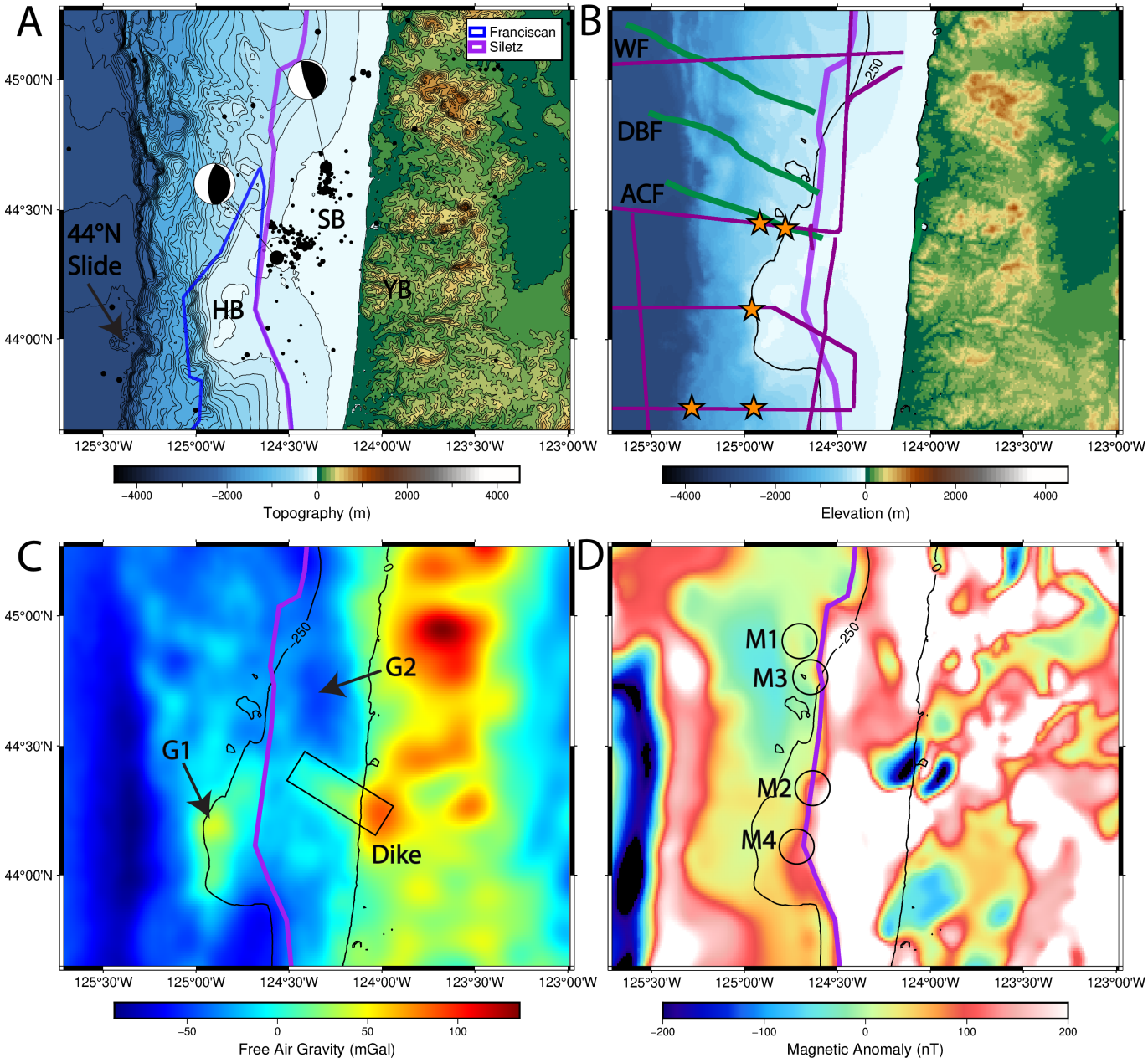


Figure 2 Maps displaying geophysical data from previous experiments within our study region. Lines denoting terrane boundaries are the same as in Figure 1. (A) Map showing topography from the Global Multi-Resolution Topography Synthesis with black contour lines every 100 m (Ryan et al., 2009). Black circles show earthquakes that occurred between 2011 and 2015 from Morton et al. (2023) and two moderate events from 2004 with focal mechanisms from Tréhu et al. (2008). Labels denote location of named shelf banks (HB: Heceta Bank, SB: Stonewall Bank) and onshore structure (YB: Yachats Basalt). (B) Green lines show strike-slip faults mapped by Goldfinger et al. (1997). WF: Wecoma Fault, DBF: Daisy Bank Fault, ACF: Alvin Canyon Fault. Thin purple lines show the CASIE21-MCS ship track and orange stars are seamounts identified using the MCS data (Carbotte et al., 2022, 2024). (C) Free-air gravity anomalies from Sandwell et al. (2014). (D) Magnetic anomaly map from Maus (2009). Potential field anomalies G1-G2 and M1-M4 were identified and discussed by Tréhu et al. (2012). (B–D) Bathymetric contours at -250 m (delineating Heceta Bank) and 0 m (marking the coastline) are shown.

model for this part of the margin. An important finding of this initial study was the variability in Siletz terrane thickness. In 1996, a second controlled-source amphibious seismic study, ORWELL (ORegon and Washington ExpLoration of the Lithosphere), collected data south of the 1989 seismic line. During this experiment, instruments were deployed along a line located at 44.6°N. These instruments spanned from west of the deformation front to the western edge of the Cascade range. The study also included two margin parallel lines, referred to as P8 and P9, over the continental shelf and helped constrain the seaward edge of Siletzia along this profile. A detailed explanation of the data quality and picking process for the 1989 and 1996 data can be found in Tréhu et al. (1994) and Gerdom et al. (2000), respectively.

2.2 2012 Data

The 2012 Ridge to Trench study (Horning et al., 2016; Han et al., 2016; Canales et al., 2017) was an active-

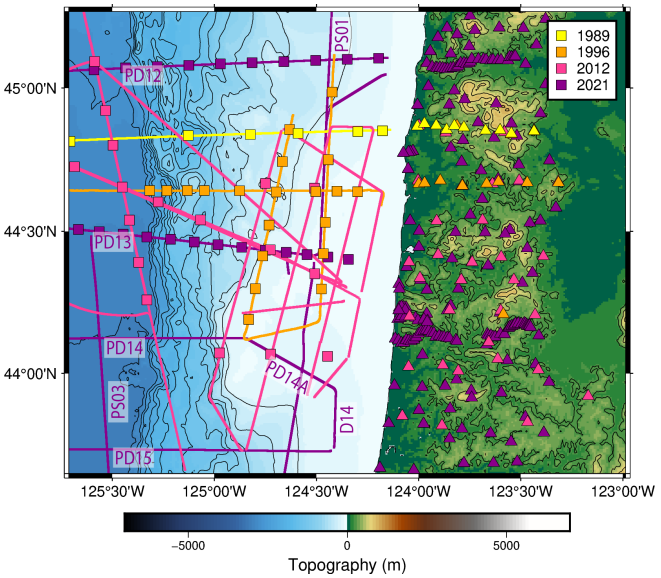


Figure 3 Map showing the experiment geometry. Lines represent the airgun shots, squares show location of ocean bottom seismometers/hydrophones, and triangles show land-based seismic stations. Airgun shot lines and seismic stations are colored by experiment year and airgun shot lines from 2021 are labeled.

source seismic experiment to image the CSZ. In this study, we utilized airgun shots and instruments located on line 1 of this study, which runs perpendicular to the margin, and line 3, which runs parallel to the margin. Line 1 was previously analyzed by Horning et al. (2016) and Line 3 by Canales et al. (2017). We also incorporated data from an add-on deployment that included 6 additional OBSs and four margin-parallel shot lines on the continental margin (Figure 3). Seismic stations were deployed throughout the coastal ranges between 43.7°N and 44.7°N to record the offshore airgun shots.

Travel times from onshore stations and 6 OBSs that were picked and previously modeled by Kenyon (2016) and Tréhu et al. (2023) were used in this study. We made additional travel time picks on 6 more OBSs located along the southernmost portion of airgun lines 1 and 3 in the Ridge to Trench Experiment to extend the Tréhu et al. (2023) model seaward. Shot spacing varied by line and ranged from 37.5 m to 500 m to accommodate the collection of multi-channel seismic data and wide-angle reflection/refraction data. Data quality for these instruments varied significantly. On the vertical component of the 2012 marine instruments, intermittent noise in the range of 6 Hz is present, which is not observed on the hydrophones. This noise was previously reported in other studies (Monigle et al., 2009), but the cause of it remains unknown. When the noise overwhelms the signal, travel time picks were made on the hydrophone.

2.3 2021 Data

In the summer of 2021, a large active-source seismic experiment called the CAscadia Seismic Imaging Experiment (CASIE21) took place, which included the collection of MCS data using a long streamer and the deployment of ocean-bottom seismometers. The CASIE21-MCS experiment collected over 5300 km of MCS data along margin parallel and perpendicular lines using the airgun array and hydrophone streamer of the R/V Langseth (Carbotte et al., 2024). The CASIE21-OBS experiment deployed OBSs at 120 sites located along 10 of the margin perpendicular lines (Canales et al., 2023). For this study, we made travel time picks on 16 of the CASIE21 OBSs that were deployed along shot lines PD13 and PD12. These instruments were located ∼8 km apart, and we utilized shots from lines PD12, PD13, PD14, PD14A, D14, PS01, and PS03, which were shot with an interval of 37.5 m. This helped constrain the crustal structure offshore and added north-south ray paths to our data set, which was dominated by east-west rays. Throughout most of the data set, the signal-to-noise ratio was high, with the exception of a few instances where previous shot noise overwhelmed the desired signal. The addition of the CASIE21-OBS data adds valuable crossing raypaths that sample the region beneath Heceta and Stonewall Banks.

As part of an onshore complementary study referred to as Cascadia2021, we installed nodal seismometers onshore to record the offshore airgun shots and extend modeling efforts in that direction (Ashraf et al., 2025). The Cascadia2021 team installed 755 Fairfield Nodal Zland 3C nodes throughout the coastal ranges of Oregon and southern Washington (Tréhu et al., 2022a). The onshore array included a grid of sites with ∼15 km spacing and 6 dense lines running approximately east to west, as shown in Figure 1C and Figure 3. The lines of nodal instruments were designed to align with the east-west shot lines of the R/V Langseth. The nodal seismometers recorded continuously for ∼35 days from late May to early July. Figure 3 shows the location of the grid sites and dense lines of nodes used in this study. The nodes within our study area recorded shots along margin parallel lines and perpendicular lines and we picked Pg, Pn, and PmP arrivals for shot line and grid site combinations with high enough signal-to-noise values. The ∼2 km spacing between nodes on the two dense lines allowed us to omit stations with poor signal-to-noise in which arrivals would be challenging to identify. We only incorporated picks for every second or third station on these lines.

The quality of the 2021 nodal data varied, but overall we estimated 90% of nodal instruments in this region had usable data. Nodes located within ∼2 km of the coast had increased noise due to the proximity of the ocean, and we were unable to make any picks on these instruments. Other sources of noise seem to occur primarily during daylight hours. Many of these nodes were located on logging properties, and we suspect this noise is due to logging operations or other sources of cultural noise. Overall, the signal-to-noise ratio for the dense lines and grid stations is good, even at offsets greater than 100 km. Similar signal-to-noise ratios and signal detection at source-receiver offsets greater than 100 km were also recorded on most of the onshore instruments during the previous experiments.

3 Methods

3.1 Picking Travel Times

We combined the four datasets and made new travel time picks on 6 additional OBSs deployed during the Ridge to Trench experiment, 16 OBSs from the CASIE21-OBS experiment, and 102 nodal instruments from the Cascadia2021 experiment. Data were filtered using a minimum phase 4th order bandpass filter between 3 and 15 Hz. Synthetic travel times generated from the existing OR2012 3D P-wave velocity model (Kenyon, 2016; Tréhu et al., 2023) and our starting model (see description below) were used to guide the identification and selection of arrival times for each seismic phase. This was particularly beneficial as some portions of the shot lines passed over basins that distorted the signal coherence.

Figure 4 shows that several crustal seismic phases were visible through the 2021 data sets. On the 2021 land stations, refractions through the continental crust, Pg, are visible on all record sections. These Pg phases can be seen up to offsets of ∼80 km. Waves bottoming out in the upper mantle, Pn, are also visible on most stations, with some Pn arrivals visible at ∼200 km offsets. Reflections off the Moho interface, PmP, are also quite clear on some record sections. In a few instances, Pn arrivals are very faint and only visible in some regions, with a significantly higher amplitude PmP phase arriving shortly after. Additionally, reflections from a shallower reflector are visible on many of the 2021 grid sites as well as in the 1996 and 2012 datasets. We hypothesize this phase may correspond to reflections from the top of the subducting crust. Pg, Pn, and PmP phases are also seen on the majority of the 2021 and 2012 OBSs. An uncertainty value was assigned for each travel time observation during the picking process. The uncertainty is an estimate of the error in visually identifying the travel time pick, locations of the source and receivers, and uncertainty due to the ray tracer.

3.2 Modeling Process

Pg, Pn, and PmP travel time picks from the four controlled-source seismic experiments were inverted with travel time tomography using the approach of Toomey et al. (1994) and Dunn et al. (2005). This method allows the user to specify several a-priori constraints and control the smoothing and penalty parameters used in the inversion. We constructed a 3D starting model defined by slowness nodes sheared vertically to hang from the topography. An initial slowness model was defined on a grid with 500 m spacing in the horizontal and vertical directions, and the model spans 231 km x 189 km x 80.5 km. Our starting model was created using the methods of Ashraf et al. (2025) and then convolved with moving averages for each 1D vertical profile to smooth out the high gradient Vp boundaries, such as the slab top and bottom. The starting model included a Moho interface defined at 500 m spacing, which spans the entire x-y plane of the model. A coherent Moho structure was generated by integrating high-resolution offshore seismic reflection data from the CASIE21 expedition (Carbotte et al., 2024) with lower-resolution onshore receiver function data from Bloch et al. (2023). Detailed methodologies for constructing this shoreline-crossing Moho are provided in Ashraf and Hooft (2026).

In this method, each iteration consists of solving the forward problem to generate ray paths and travel times for the current model, followed by the inverse problem. The forward problem uses the Moser (1991) shortest path algorithm to calculate the travel times through the slowness model. One advantage of the Toomey et al. (1994) approach is that it calculates the time through the water column using a finer bathymetry grid spacing than it does for the remainder of the forward problem. The travel times through the water column were calculated using a 100 m x 100 m grid, allowing the slower path through the water column and the seafloor entry point to be calculated more accurately. Next, the code calculates the shortest travel time to each node within the model space and determines the time for a shot to reach each receiver. Following this step, the inverse problem updates the slowness model and Moho interface (Dunn et al., 2005). For the inverse problem, we use a coarser perturbational grid spacing of 1 km in all directions. The inverse problem solves the equation $\mathbf{d} = \mathbf{Gm}$. $\mathbf{d}$ is a vector of observed minus calculated travel times that the inversion seeks to minimize. $\mathbf{G}$ is the Frechet matrix containing partial derivatives of the travel times with respect to each model parameter. Smoothing and damping constraints are also included in the $\mathbf{G}$ matrix. $\mathbf{m}$ is a vector containing all of the model parameters for the velocity model and Moho interface.

We tested different penalty parameters and smoothing values to find our preferred model. We ran 8 iterations of the inversion using the jumping method (Shaw and Orcutt, 1985; Toomey et al., 1994). The starting model produced an initial RMS misfit of 918 ms for Pg arrivals, 534 ms for Pn arrivals, and 554 ms for PmP arrivals. Following 8 iterations, the RMS misfit values decreased to 142 ms, 140 ms, and 130 ms for Pg, Pn, and PmP arrivals, respectively. Additionally, we tested the sensitivity of the inversion to reasonable variations in pick uncertainties and weighting parameters. Although the resulting RMS misfits varied modestly, the principal velocity structures and geologic interpretations remained unchanged. Details of these tests are provided in Supplementary Table S2.

4 Results

Here, we describe the features that are well resolved within the overriding plate, followed by those on the subducting plate and the Moho interface. Depth averages, east-west and north-south cross-sections through our final 3D tomographic P-wave velocity model are shown in Figures 5, 6, and 7, respectively. Earthquake hypocenters from Morton et al. (2023) within 6 km of each transect are projected onto the cross-sections. The derivative weight sum (DWS), which measures the contribution from each ray to the velocity-travel time derivatives at each model node (Toomey and Foulger, 1989), was used to mask the portion of our 3D model with insufficient ray coverage. We mask regions of our

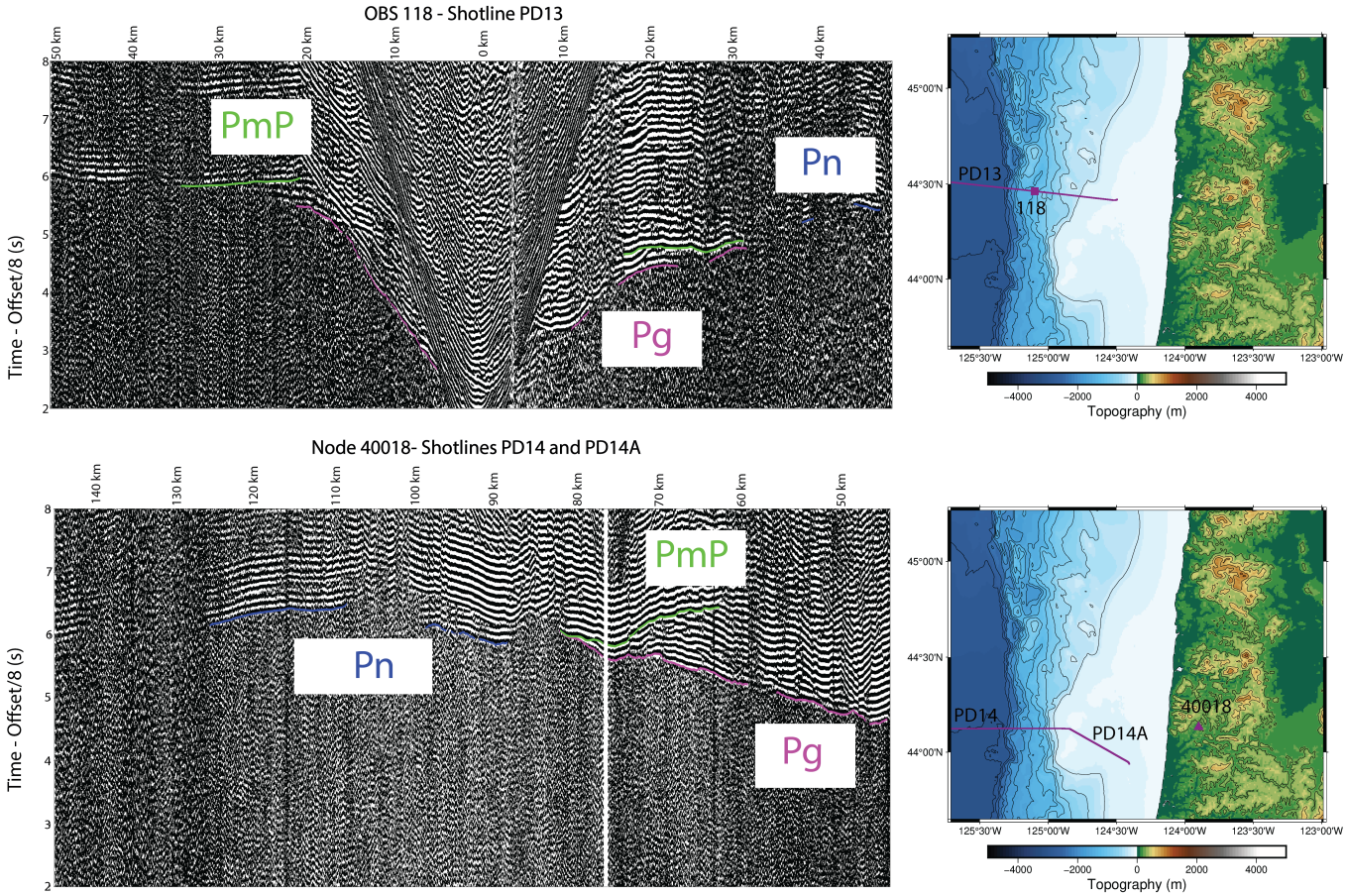


Figure 4 Examples of record sections with good quality data from the 2021 experiments. Top panel shows airgun signals from PD13 recorded on OBS 118. Bottom panel shows signals from lines PD14 and PD14A recorded on seismic node 40018. Maps show location of the shots and stations shown in the record sections.

velocity model with DWS values less than 1. Overall, our model has good 3D ray coverage, spanning from the deformation front to landward of the coast.

4.1 Seismic Velocity Structures in the Overriding Plate

4.1.1 Accreted Terranes

The Vp structure of the overriding plate reveals several distinct velocity anomalies. In the eastern part of our model, we identify a high-velocity body with values exceeding 5 km/s. Based on both its location and velocity characteristics, we interpret this feature as the Siletz terrane. Previous work shows that velocities within Siletzia vary spatially (Gerdom et al., 2000), with an average of about 5.5 km/s in south-central Cascadia (Ashraf et al., 2025). In the outer forearc, overlapping velocities make it difficult to distinguish Siletzia from the downgoing plate. To address this, we use the combined pattern of velocity and thickness, together with the structural boundary inferred from aeromagnetic data. Supplementary Figure S1 shows the thickness of material between the 5.5 km/s isovelocity surface and the inferred top of the crust, located 6 km above the final Moho. Regions containing more than 3 km of material with >5.5 km/s above the inferred top of the subducting crust align most closely with the seaward edge of Siletzia mapped by Wells et al. (2014). The imperfect correspondence between this thickness-based boundary and the magnetic boundary suggests lateral variations in terrane thickness. Accordingly, in Figures 6–7, we use the 5.5 km/s contour, restricted to regions where it overlies more than 3 km of material with Vp $\geq$ 5.5 km/s, to approximate the limit of the terrane boundary.

Within the region of the structurally defined seaward edge of Siletzia (SES), the 5.5 km/s contour also highlights along-strike changes in backstop geometry. North of 44.45°N, the inferred Siletzia edge dips westward, becoming nearly vertical around 44.40°N. South of 44.20°N, the dip angle decreases, and the boundary transitions to a shallow westward dip. We do not observe an obvious change in Vp structure at the previously interpreted boundary between the Siletz and Franciscan terranes. Although we have good ray coverage in the accretionary prism, it remains difficult to identify a clear boundary between the prism and accreted terranes. This limitation stems from the overlapping lithologies shared by the prism and terrane sediments, which make them challenging to distinguish.

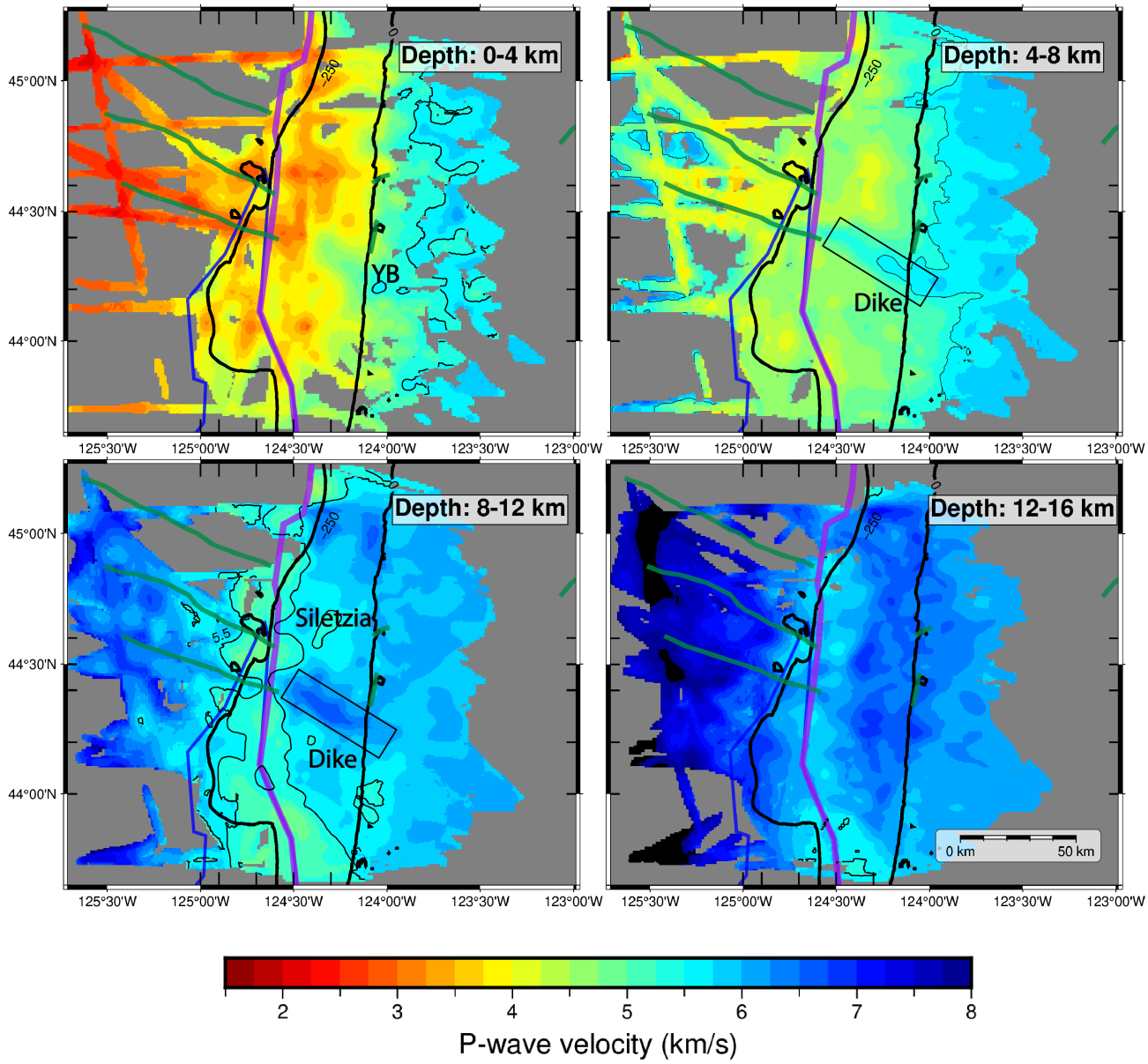


Figure 5 Average P-wave velocities at selected depths. Thin black contours denote the 5.5 km/s isovelocity surface. A rectangle outlines a high-velocity feature interpreted as a dike. Short black lines along the map edges mark the locations of the east–west and north–south cross sections shown in Figures 6 and 7. See Figure 2 for symbol definitions.

4.1.2 Dike

Within the Siletz terrane, we observe a distinct region of higher velocities. This feature corresponds to a mafic dike identified by Tréhu et al. (2023) and is visible as a free-air anomaly gravity high in Figure 2. The dike is visible in Figure 5 and extends from 44.4°N/124.6°W to 44.2°N/124.0°W in our model. The feature has velocities of approximately 5-7 km/s and is ∼7 km tall. At its base, located at ∼9 km depth, it is ∼15 km wide and narrows to 8 km as it approaches the surface; it is 50 km long. In our model, we find this anomaly is slightly wider at the base and longer than noted in Tréhu et al. (2023). The orientation of this feature is similar to that of the ACF and extends from 10 km southeast of the fault to approximately 15 km east of the coastline, beneath where the Yachats Basalt is exposed onshore. The additional station coverage added by this study better constrains the southeastern side of this feature at shallow depths, revealing that within the uppermost 4 km, the dike's high velocities are concentrated at the southeastern end of the anomaly, coincident with the Yachats Basalt outcrop.

4.1.3 Low Velocity Zones

The model shows a zone of low velocities that coincides with the mapped surface expression of the ACF (Goldfinger et al., 1997) in Figure 5, Figure 7, and Supplementary Figure S2. The low velocities are observed in the upper 3-5 km of the overriding plate or accretionary wedge. Supplementary Figure S2 shows that these velocities range from 0.5 to 1 km/s lower than the surrounding velocities in some regions, including the areas surrounding the Daisy Bank Fault. The largest differences in velocity surrounding the ACF are seen clos-

est to the surface, and changes in Vp are minimal within the subducting plate crust. Low velocities could be the result of fluid flowing through the fault (Philip et al., 2023) or a damage zone around the fault (Hole et al., 2001; Allam and Ben-Zion, 2012). As noted by Tréhu et al. (2023), there is also a shallow low-velocity zone corresponding to a north-south trending basin within the larger Newport Basin that is at least ~8 km deep, ~20 km wide, and ~40 km long.

4.2 Subducting Plate Moho

The subducting plate Moho is shown in Figure 8A masked based on the bounce points of the PmP reflections. Although PmP coverage is limited, we observe some notable changes in Moho geometry in regions where we have adequate ray paths (Supplementary Figure S3). The model reveals that the Moho becomes shallower south of the ACF by several kilometers, in agreement with Carbotte et al. (2024). Supplementary Figure S3 illustrates that the Moho directly south of the ACF is shallower than the Tréhu et al. (2023) Moho yet deeper than the top of the subducting crust interface from Carbotte et al. (2024), which is shifted 6 km downward to approximate the Moho. East of the ACF, the Moho dips more steeply around the seaward edge of the Siletz terrane (Figure 6). Between the seaward edge of Siletzia and the coastline, the Moho steepens ~1.5 km over a region of ~70 km north-south, which we attribute to the increased upper plate load of the dike above. This deflection is smaller than that reported by Tréhu et al. (2023) but follows a similar spatial pattern. Differences between the amplitude of the deflection in this study and Tréhu et al. (2023) may be due to different smoothing and/or damping parameters applied during the Moho surface inversion. Interestingly, the maximum Moho deflection is offset by ~15 km to the south of the location of the upper-plate dike.

4.3 Topography of the Subducting Plate

To identify the topographic relief on the subducting slab, we looked at slices of the final Vp model at different heights above the Moho interface. We find nine circular regions of higher velocity that are labeled S1-S5, G1, G2, M2, and M4 in Figure 8B. Given that seismic tomography lacks the vertical resolution needed to distinguish the up to ~1 km separation between the megathrust fault and the top of the subducting crust identified in earlier MCS work (Carbotte et al., 2024; Han et al., 2016), we examine velocity slices relative to our inferred top of crust surface, located 6 km above the subducting plate Moho. Many anomalies appear within 1 km above the inferred top of the crust. In this study, we discuss only those located in well-resolved parts of our model and exclude anomalies where ray coverage is poor and the lateral extent or shape of the anomaly cannot be resolved. We also focus on high-Vp anomalies situated seaward of the Siletz terrane except where independent evidence justifies further examination, as with anomalies M2 and G2. This is because the Siletz terrane generates high velocities that can smear downward into the top of crust, creating artificial high-Vp features. Additionally, we classify small, circular, high-velocity

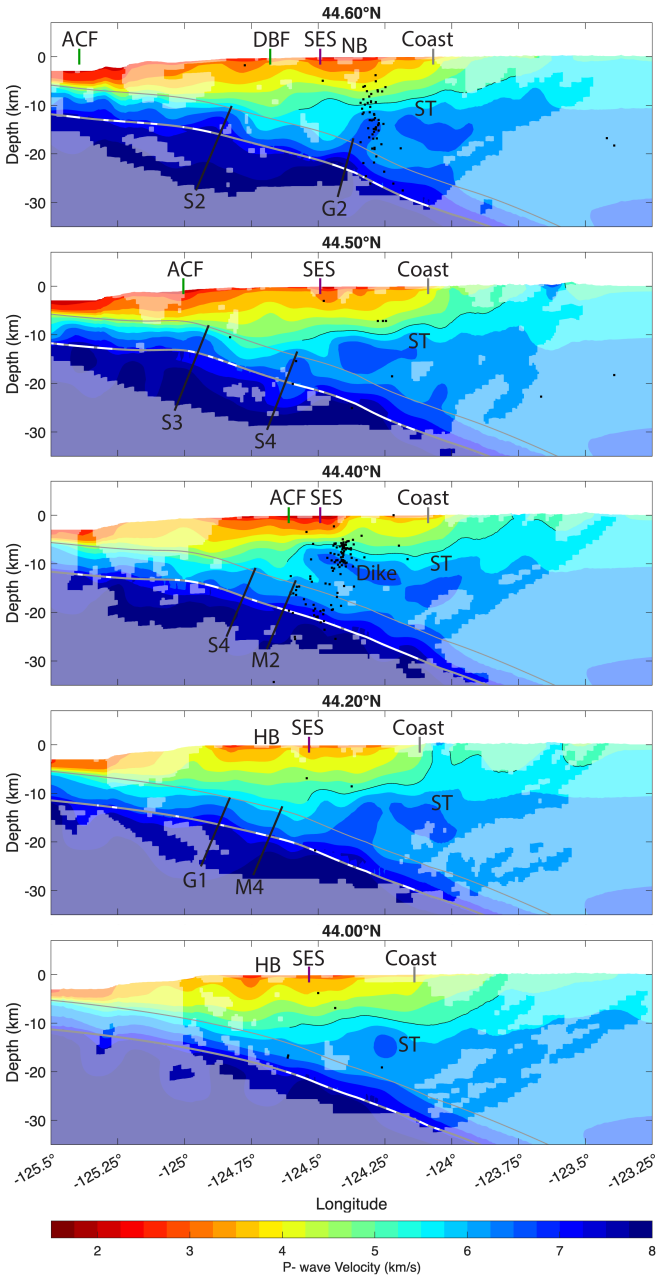


Figure 6 East-west cross-sections through our final P-wave velocity model. A transparent mask is applied to regions of our model that are poorly resolved with a Derivative Weight Sum (DWS)<1. The thin black line is the 5.5 km/s contour which we use to approximate the seaward edge of Siletzia. The thicker gray line represents our final Moho and is overlaid by white where the Moho is resolved by PmP travel times. A thin gray line is plotted 6 km above the final Moho to serve as a reference for the approximate top of the subducted oceanic crust. Labels indicate the intersection between the cross-sections and the following features: HB: Heceta Bank, SB: Stonewall Bank, NB: Newport Basin, SES: Seaward edge of Siletzia from aeromagnetic data, ST: Siletz terrane, DBF: Daisy Bank Fault, ACF: Alvin Canyon Fault, WF: Wecoma Fault, Coast: the coastline, and S1-S5, G1, G2, M2, M4: proposed subducting seamounts. Earthquakes within 6 km of each cross-section are plotted as black circles (Morton et al., 2023).

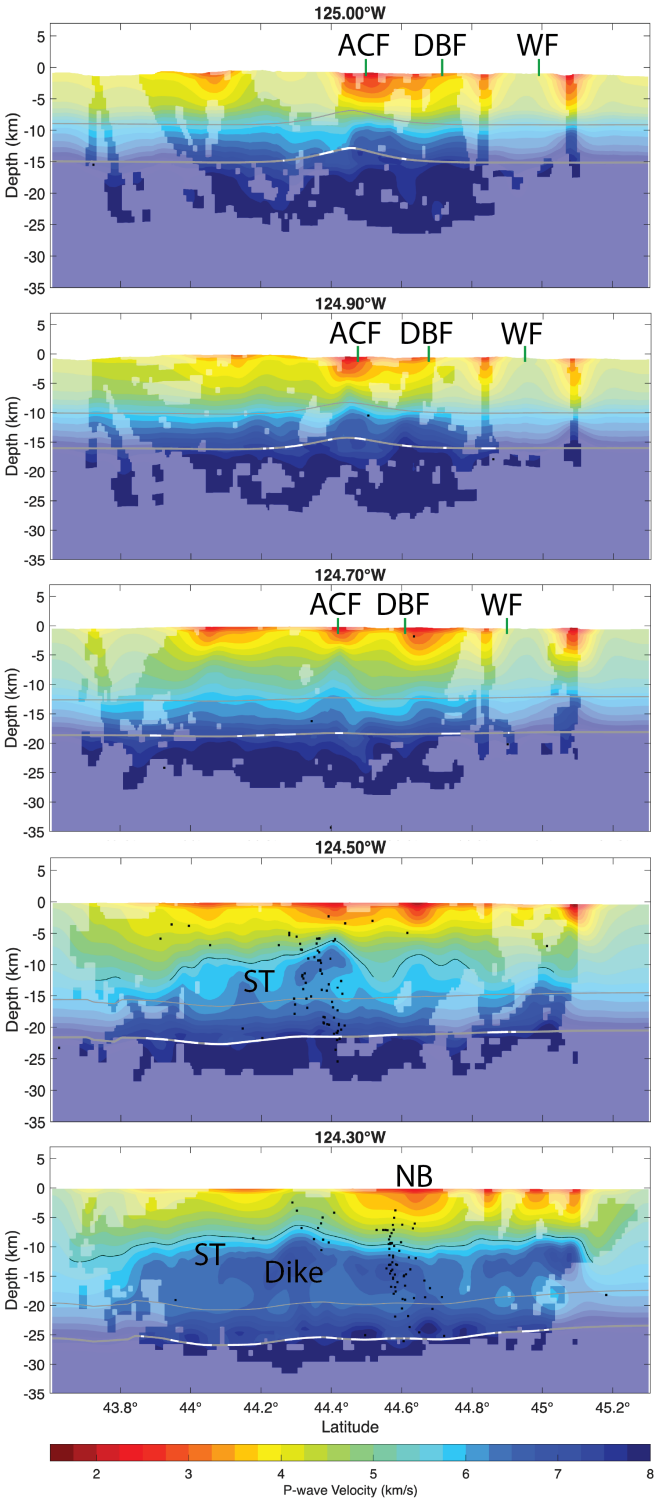


Figure 7 North-south cross-sections through our final P-wave velocity model. See Figure 6 for an explanation of the symbols and labels.

anomalies within roughly 1 km above the crustal top as seamounts when their amplitude and geometry closely match anomalies independently confirmed as subducting seamounts in potential-field data and multichannel seismic (MCS) images.

Here, we describe these anomalies from north to south, and where seamounts coincide with potential field anomalies, we refer to them by the labels given to the anomalies in Tréhu et al. (2012). Tréhu et al. (1994) identified a seamount S1 based on 2D modeling of seismic refraction data. Since our new travel time picks do not provide additional insights into this anomaly, we do not discuss S1. South of S1, we see a top of crust anomaly that coincides with magnetic anomaly M1, but poor ray coverage in this region does not allow us to assess the size or shape of the anomaly. A top of crust anomaly located at approximately 124.8°W and 44.6°N, which we refer to as S2, is better constrained by our data. This feature is ~10 km wide, and the high velocities are concentrated directly west-southwest of a quasi-circular bathymetric bump with a depth of 250 m. A broad, elongated region of high velocity is located at the top of the subducting crust beneath the sedimentary basin proposed to be associated with seamount G2.

Three high-velocity anomalies are located at the top of the subducting crust from 44.5°N to 44.35°N. Features S3 and S4 were observed by Carbotte et al. (2024) along MCS line PD13 as shown in Figure 2. In our model, anomaly S3 is located southwest of a small circular bathymetric high just seaward of Heceta Bank. The ~6 km wide anomaly is composed of velocities ranging from 5.25 to 5.75 km/s, which contrast the surrounding velocities of 4.5 to 5.25 km/s (see Figure 8). Feature S4 is approximately 10 km wide at its base and is located down dip of a low-velocity anomaly associated with the ACF and directly landward of the -250 m bathymetry contour. A third high-velocity anomaly, M2, is located ~6 km southeast of S4 and landward of the Siletz terrane boundary. This feature was not previously identified through MCS data, as the CASIE21 ship track ended north of this anomaly, but it does correspond with a magnetic anomaly. In our model, this high-velocity anomaly has a basal diameter of 7 km, but the anomaly appears to be part of a larger high-velocity anomaly associated with Siletzia. Anomalies S3, S4, and M2 are all located on the south side of the ACF.

Two more circular high-velocity anomalies, G1 and M4, are seen at the top of the subducting oceanic crust near the edge of Heceta Bank. The westernmost anomaly, G1, coincides with a prominent free-air gravity high and is located slightly north of an anomaly observed in the MCS data along shotline PD14 (Carbotte et al., 2024). It is possible that these are the same feature, and in our model, the high velocities are smeared northward. M4 is located beneath Heceta Bank and corresponds with a magnetic anomaly. Both features are located around 44.20°N and can be seen in cross-section in Figure 6. In our model, G1 is 5 km wide, with velocities of up to 5.75 km/s. M4 is significantly larger, with higher velocities. This feature is elongated to the east and west, with velocities of up to 6 km/s spanning 20 km in diameter. Some elevated velocities are seen at the southern edge of Heceta Bank, but a lack of ray coverage in this area prevents us from characterizing this region. The gravity high associated with G1, shown in Figure 2, appears to extend from the velocity anomaly S4 southwest to G1, where it is highest, and to the southern edge of Heceta Bank. It is also possible, based on the limited resolution of the free-air gravity, that anomaly M4 is contributing to the gravity high. South of Heceta Bank, a high-velocity anomaly, S5, is not well constrained in our model but coincides with a seamount observed by

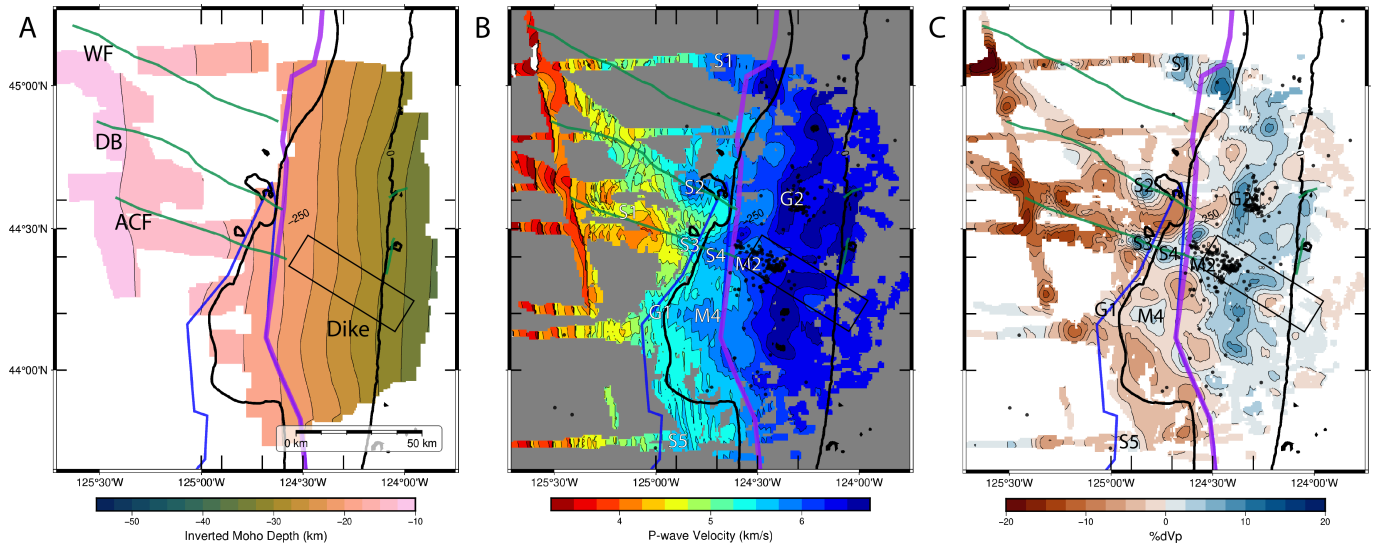


Figure 8 (A) Moho interface inversion results, with contours at 2.5 km intervals. (B) Average P-wave velocity 6–7 km above the final modeled Moho interface. Note that a different color scale is used here than in previous velocity figures to better emphasize variations within this region. (C) Velocity perturbations relative to the starting model, also averaged over 6–7 km above the final Moho interface. Symbols are the same as in Figure 2 and Figure 5. The purple line marks the seaward edge of Siletzia (Wells et al., 2014); high-velocity anomalies are interpreted as seamounts only west of this boundary, unless supported by independent geophysical evidence. Earthquakes from Morton et al. (2023) are shown as filled black circles in panels (B) and (C).

Carbotte et al. (2024) along MCS line PD15. It is ∼10 km wide in the east-west direction, with velocities between 5.5 and 5.75 km/s in our model.

4.4 Hypothesis-Based Resolution Tests

To determine whether we could recover these features with our experimental geometry, we ran a series of hypothesis-based resolution tests. We constructed synthetic models with simplified, high-velocity features placed on top of the subducting crust. We calculated synthetic arrival times for these models using only the shot-station pairs with travel-time picks. Then, we ran these synthetic arrival times using the same starting model and inversion parameters employed for our preferred tomographic model. Figure 9 shows the recovery of anomalies S2 and G1 in our hypothesis tests. These tests show that we can recover features comparable in size and velocity perturbation to those in our final inverted model; however, the features are consistently under-recovered in our tests. The high velocities are smeared into the surrounding region, suggesting that the true features are either larger or faster than those in our final model. This degree of under-recovery and smearing is expected given the raypath geometry and smoothing constraints used in the inversion, which limits the sharpness of resolvable boundaries. Despite these limitations, the tests demonstrate that we can confidently identify the presence and general location of these features. Additional figures showing the results of our resolution tests are presented in Supplementary Figure S5 and demonstrate a similar recovery pattern, illustrating how features can become smeared.

When the dimensions of our interpreted seamounts are compared with those imaged by Carbotte et al. (2024), we find that features S3 and S4 in our model have

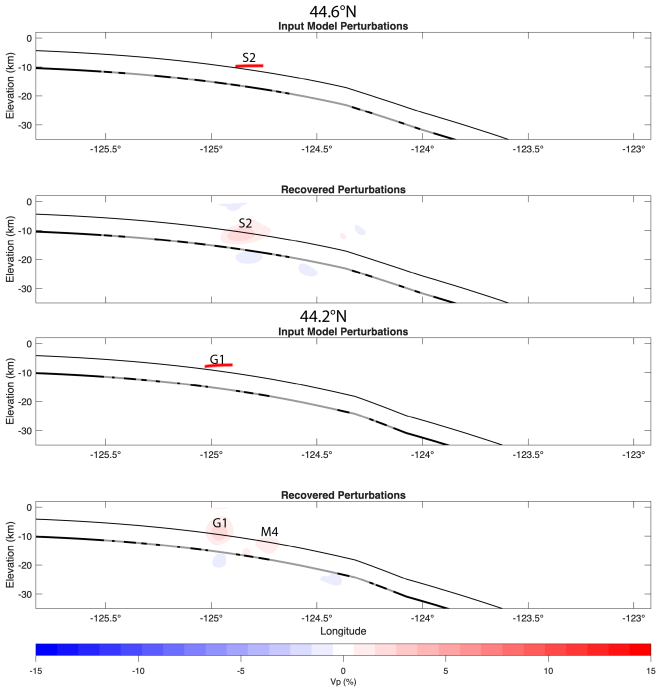


Figure 9 Hypothesis test assessing the ability to recover high-velocity anomalies on top of the subducting crust. Panels 1 and 3 illustrate east–west cross sections through the input model containing perturbations designed to replicate anomalies S2 and G1. Panels 2 and 4 show the corresponding recovered perturbations. M4 shows up in the recovered panel because it is smeared from just south of this cross section. The thick black line denotes the Moho interface, with gray shading indicating regions that are well resolved. The thin black line represents the approximate top of the subducting crust, positioned 6 km above the Moho.

substantially greater apparent heights than their corresponding structures in the MCS data. Carbotte et al. (2024) reports that the two seamounts along line PD14 are 1–2.5 km tall, whereas in our tomography model, the associated high-velocity anomalies extend several kilometers above the inferred top of the crust. This discrepancy suggests two possibilities: either the CASIE21 MCS line did not intersect the exact centers of the seamounts and therefore underestimated their true dimensions, or the seamount velocities in our model are smeared upward and broadened, causing the features to appear larger than their actual size. Figure 9 illustrates this smearing effect and shows that 1 km tall anomalies can be smeared, resulting in an anomaly that is three times taller than the initial input anomaly. Supplementary Figure S4 shows that the 2021 MCS shotlines crossed approximately over the centers of seamounts S3 and S4 in our model. This geometry supports our interpretation that the excess vertical extent in our model is primarily an artifact of velocity smearing rather than an indication of a larger true seamount size.

5 Discussion

5.1 Deformation in the Accretionary Wedge

5.1.1 Scars and Slides at the Trench

High-resolution bathymetry data reveal scars and slides at the deformation front (Tréhu et al., 2022b), potentially caused by seamount subduction (Tréhu et al., 2022b; Babendreier, 2023), and significant regions of uplift along the continental shelf of unknown origin. Scars related to seamounts passing through the deformation front have been documented along the Costa Rica margin (von Huene et al., 2000) and in laboratory sandbox models (Dominguez et al., 1998). In Supplementary Table S3, we compiled a list of features in this region and their ages based on the literature to better understand the relationship between faulting, subducting topography, and the complex bathymetry along this margin. Additionally, we calculated the trajectory of each potential seamount through time. In this calculation, we assumed the deformation front was stationary during this time period. The trajectories of these seamounts are shown in Figure 10B, and the approximate times they crossed the deformation front are listed in Supplementary Table S4. Plate motions were calculated for the Juan de Fuca plate relative to the Oregon block by vector addition of Juan de Fuca motion relative to stable North America (DeMets et al., 2010) and Oregon block motion relative to stable North America (McCaffrey et al., 2007). A comparison of Juan de Fuca–North America and Juan de Fuca–Oregon block plate motions is provided in Supplementary Figure S6.

Obvious disruptions in the deformation front are seen at 43.64°N, 43.70°N, 44.0°N, 44.13°N, 44.25°N, 44.58°N and 45.08°N. The largest of these is the 44.0°N blocky slide, which is composed of a series of slides. Age estimates for these events vary significantly depending on the dating technique used (see Supplementary Table S3). Ages from biostratigraphic analysis yield significantly younger ages than those from a constant sedimentation rate (Babendreier, 2023). Our calculations suggest that five seamounts (G1, G2, S3, S4, and M2) have passed through the deformation front around 44.0°N or 44.13°N. A potential seamount associated with the G2 anomaly would have crossed the deformation front 3 mya, whereas G1 passed through the same region only 900 kya. The 44°N slide complex described by Tréhu et al. (2022b) includes a deeply buried slide dated to 1.3 myr at 44.13°N and a younger series of slope failures between 44 and 119 kya, all of which could be caused by the subduction of the seamounts in our model (Babendreier, 2023; Tréhu et al., 2022b). This chronology implies that, if seamount subduction is responsible for these failures, there is a substantial time delay between seamount passage and slope collapse. Repeated episodes of uplift and subsidence generated as these seamounts crossed the deformation front may have destabilized an area already prone to slope instability, producing the series of blocky slides observed near 44°N.

Proposed seamount S1 crossed the deformation front ∼1.8 mya just north of a scar in the deformation front at ∼44.58°N that has not been dated. The trajectory of the seamount suggests that it may have caused this indentation at the deformation front and may have led to a significant slump located ∼20 km east of the trench along the seamount's trajectory. Similarly, the trajectory of proposed seamount S2 also lines up with the deformation seen in Figure 10. A more comprehensive list of ages for the deformation near the trench, particularly north of the 44.0°N slide, is needed to understand whether seamounts S1 and S2 could be responsible for distinct regions of deformation at the trench. Our new observations of likely subducted seamounts and their association with the series of slides around 44°N support Tréhu et al. (2022b)'s hypothesis that the subduction of a seamount province could be responsible for the slides that are unique to the south central Oregon portion of the Cascadia margin.

5.1.2 Uplift of Heceta and Stonewall Bank

This segment of the margin contains two prominent banks shown in Figure 2: Heceta Bank and Stonewall Bank. Heceta Bank is an uplifted erosional platform on which Miocene-age folds are exposed at the seafloor. Uplift has been attributed to the subduction of a topographic high (Fleming and Tréhu, 1999). At present, it is characterized by extensive methane venting and the resulting formation of carbonate structures (Torres et al., 2009). The seaward edge of Siletzia, as indicated by magnetic anomalies, falls within Heceta Bank but does not have any seafloor expression (McNeill et al., 2000). Stonewall Bank represents the northeastern continuation of Heceta Bank and includes a distinct NNW-striking topographic anticline, known as the Stonewall Anticline, that shows signs of Holocene activity (Yeats et al., 1998).

The uplift history of these bathymetric highs is not well constrained, but several mechanisms may have contributed to their development, including regional uplift associated with dike emplacement and more lo-

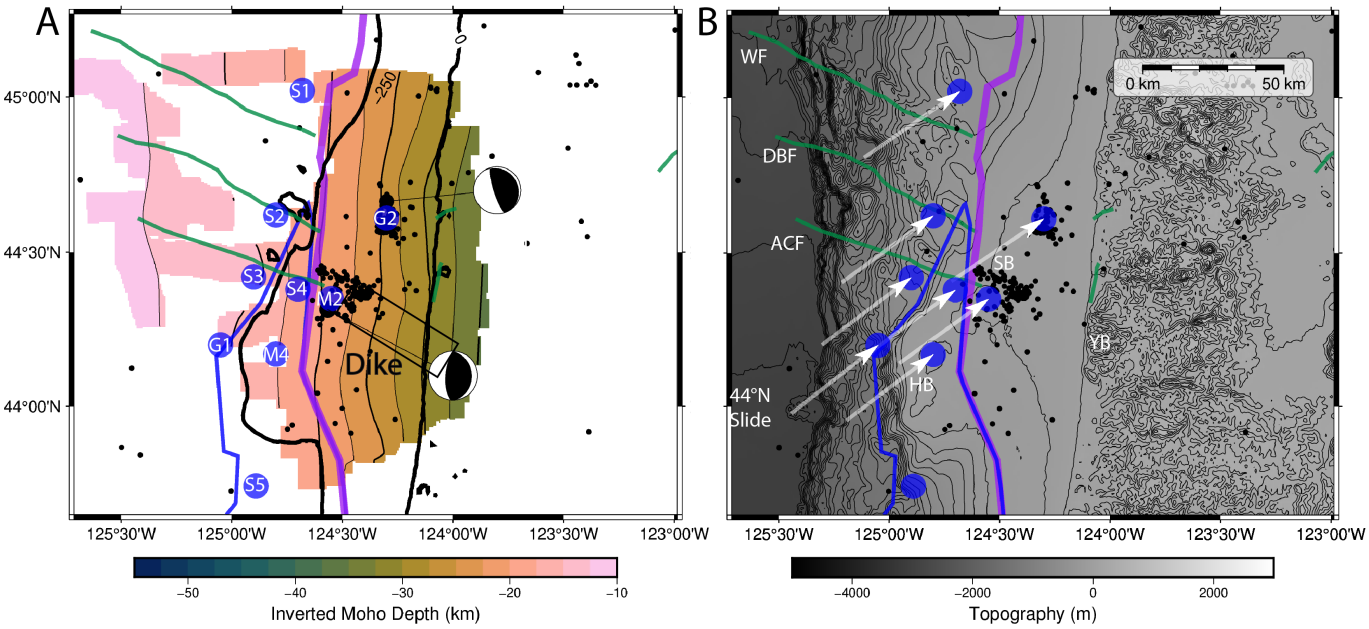


Figure 10 Summary of the spatial distribution of features in our model and their relationship to previously mapped structures. Blue circles denote proposed seamounts identified in our final velocity model, and black circles show earthquakes from Morton et al. (2023). Green lines mark the Wecoma, Daisy Bank, and Alvin Canyon Faults (WF, DBF, and ACF). (A) Final depth estimates for the subducting plate Moho. Focal mechanisms for the two moderate earthquakes that occurred in 2004 are from Tréhu et al. (2008). The black rectangle indicates the extent of the mafic dike in our model. (B) Map of high-resolution topography from the Global Multi-Resolution Topography Synthesis (Ryan et al., 2009). The locations of the 44°N slide, Heceta Bank, Stonewall Bank and the Yachats Basalt outcrop are labeled. White arrows show the approximate trajectories of the seamounts over the past 1.5 myr based on the motion of the Juan de Fuca plate relative to the Oregon block, calculated using plate motions from DeMets et al. (2010) and McCaffrey et al. (2007).

calized deformation driven by seamount subduction. The formation of the dike may have led to broadly distributed uplift of this region 37 million years ago. More recently, seamount subduction may have altered the bathymetry at shorter spatial scales. At present, M2 and G2 are located beneath Stonewall Bank and are associated with clusters of seismicity (Tréhu et al., 2023). M2 abuts the western edge of the Siletz terrane magnetic anomaly and a small "peninsula" of relatively high elevation, as shown in Figure 2A by the -100 m depth contour, which appears to follow the subduction trajectory of M2. Tréhu et al. (2023) noted that the location of Stonewall Anticline between the two seismicity clusters is intriguing and suggested that this may reflect coupling between the upper and lower plates. Heceta Bank also overlies the proposed seamounts M4 and S4, which are within 15 km of the -250 m bathymetric contour used to define the bank. Seamount M4 coincides with one of the two smaller circular bathymetric highs on top of Heceta Bank and velocity model coverage is poor in the region corresponding with the southern bump. We hypothesize that the subduction of this seamount could produce additional uplift directly above the feature or downdip of the feature's current position as they deform the accretionary wedge, acting as plows.

5.2 Seismicity

Cascadia lacks the frequent microseismicity observed at other subduction zones; however, the central Oregon margin hosts two prominent clusters of small- to moderate-sized earthquakes. The southern cluster is located at the intersection of three features in our model: the ACF, a subducting seamount (M2), and the seaward edge of a mafic feeder dike embedded within the Siletz terrane. Carbotte et al. (2024) attributed the observed seismicity to the complex tectonic interactions at the intersection of the ACF and an east-west trending shelf structure. Based on the Morton et al. (2023) seismic catalog, seismicity does not appear to be distributed along the ACF; rather, it is clustered down dip of the M2 seamount we imaged and within the Siletz terrane. Tréhu et al. (2008) calculated a focal mechanism for the Mw 4.9 earthquake that occurred in 2004 within this cluster. Additionally, steeply dipping thrust mechanisms are reported for two Mw 3.8 earthquakes occurring in 2012 (Tréhu et al., 2015) and in 2017 (Tréhu et al., 2018), both located near the southern cluster of seismicity.

Based on the thrust mechanisms and the localized nature of the seismicity, which clusters above the subducting plate Moho and within the overriding plate, we speculate that the seismicity occurs as the M2 seamount subducts and encounters the Siletz terrane backstop or potentially the denser mafic dike. The spatial relationship between the seismicity and the imaged seamount, together with the associated focal mechanism, is consistent with seismicity linked to seamount subduction along the central Ecuadorian margin (Segovia et al., 2018). Similar spatial patterns are observed along the

northern Hikurangi margin (Shaddox and Schwartz, 2019; Arai et al., 2020; Todd et al., 2018), where seismicity and tremor are concentrated downdip of subducting seamounts along the plate boundary and within the overriding plate. If the seismicity were caused by the fault, we would expect it to extend along the fault and to observe strike-slip focal mechanisms. A second cluster of seismicity produced a Mw 4.7 earthquake in 2004 with a similarly oriented thrust mechanism (Tréhu et al., 2015) and coincides with a free-air gravity low, G2, caused by a sedimentary basin. The similarity of the focal mechanisms for the two largest recorded events in these clusters could suggest a common origin. As both clusters are located near proposed topographic highs along the top of the subducting crust, and only M2 is near a known fault, we propose that the seismicity associated with both clusters can be attributed to seamount subduction, confirming the inference of Tréhu et al. (2012) based on magnetics.

5.3 Interface Roughness and Plate Coupling

5.3.1 Asperity Development and Rupture Barriers

We hypothesize that the rough top of the subducting crust and prominent faults between 44.0°N and 45.0°N alter the stress state within the seismogenic zone and contribute to the patterns of Cascadia megathrust segmentation. Changes in slab geometry and topography on top of the subducting crust can contribute to a rough subduction interface. This roughness can directly shape megathrust geometry where the two surfaces coincide or produce more subtle changes to the fault interface when the megathrust lies above the top of the crust. The change in Moho depth attributed to offsets along the ACF and a depression caused by a dense mafic feeder dike creates significant changes in Moho depth over a small region. Additionally, the nine topographic highs we observe on top of the subducting Juan de Fuca plate and an additional seamount seen by Carbotte et al. (2024) where we lack adequate ray coverage create numerous small-scale heterogeneities.

Studies suggest that segments with a rough subducting plate interface host smaller earthquakes compared to segments with smoother interfaces, either due to a lack of topography or a thick sediment cover (Bassett et al., 2025). A rough plate interface may prevent large continuous asperities from forming and instead result in a series of smaller locked patches (Bassett et al., 2025). This leads to fewer great earthquakes and an increase in smaller events. This phenomenon has been observed in regions with roughness associated with subducting seamounts (Wang and Bilek, 2014) as well as with bending faulting (Shillington et al., 2015). Carbotte et al. (2024) identify the ACF system as a region of locally rough top of crust and a rough plate interface that crosses the margin. Based on the spatial correlation with margin segmentation indicators, they propose that this is a possible segment boundary. Consistent with this interpretation, our Vp model shows that the ACF cuts through at least the upper portion of the subducting crust and extends into the accretionary wedge, where it likely inhibits the formation of large, coherent asperities. Our results suggest that, in addition to the ACF and the seamounts imaged by Carbotte et al. (2024), several additional seamounts are likely present in this region, further enhancing the roughness of the subducting plate and reinforcing the interpretation that this region may act as a persistent segmentation boundary. If the paleoseismic rupture record for the CSZ is accurate, it appears that these seamounts and sharp changes in slab geometry may have previously arrested large ruptures in the central Oregon forearc. Four megathrust earthquakes recorded in the paleoseismic record have terminated between 43.5°N and 45.0°N (Leonard et al., 2010).

5.3.2 Fluid Flow and Aseismic Creep

There are a number of features in our model that we suspect alter the pore fluid pressure in this region of the margin. The subducting seamounts in this region may introduce water into the forearc which is otherwise characterized by a dry slab (Canales et al., 2017). Chesley et al. (2021) showed that seamounts can carry 3.2–4.7 times more water into the forearc compared to smooth oceanic crust. With ten potential seamounts subducting in this region, this could cause a substantial increase in water content. These fluids are released around the top of crust and into the overriding plate. The development of overpressures depends on the permeability of the surrounding rock. A magnetotelluric imaging study found that the Siletz terrane may block additional fluids from traveling into the backstop, instead causing them to remain above the top of crust and flow up dip (Egbert et al., 2022). The change in dip angle of the seaward edge of Siletzia could change how fluid builds up along the top of crust.

Faults may also provide an important pathway for fluid drainage both from the subducting oceanic crust and subducting seamounts. A warm seafloor seep, Pythia's Oasis, is located near the ACF. Geochemical analyses combined with thermal models for the region suggest that the source of the water is located at or near the megathrust, and Philip et al. (2023) hypothesize this water is draining from the ACF. The low velocities surrounding this fault in our model could result from fluids draining along the ACF. More research is needed to quantify how much water is released as these seamounts subduct and how much of this water drains through the accretionary wedge and strike-slip faults.

Regions with more subducting plate relief are associated with lower coupling and aseismic creep (Bassett and Watts, 2015; Wang and Bilek, 2014), and fluids are commonly invoked to explain this. A lower slip deficit rate is observed throughout this region (Schmalzle et al., 2014; Lindsey et al., 2021), which may suggest that this patch of rough crust from the ACF and seamounts is decreasing the coupling on the plate interface and promoting interseismic creep. This would support Wang and Bilek (2014)'s correlation between creeping segments with low coupling ratios and rugged subducting crust. Saffer (2017) found that regions of the megathrust with elevated pore pressures coincide

with regions of aseismic slip and reduced coupling. It is possible that the subducting topography in this area results in elevated pore pressures along the plate interface, which promote aseismic slip.

6 Conclusion

We use ∼418,500 Pg and Pn and ∼76,300 PmP arrival time picks from over three decades of active-source shore-crossing experiments to produce a new 3D P-wave velocity model for the central Oregon forearc, including a Moho interface between 43.6°N and 45.2°N. This model allows us to examine 3D variations within this portion of the margin, including the accretionary wedge, static backstop, and subducting plate. We compare the structures found in our model to other geophysical datasets, including high-resolution bathymetry and seismic catalogs, to understand the deformation history and ongoing deformation patterns in this region. We discuss how each of these features and the interaction between them might contribute to a megathrust segment boundary around 44.5°N (Carbotte et al., 2024; Walton et al., 2021).

In our model, we see evidence for the Alvin Canyon Fault, the Siletz terrane, a mafic dike, and 9 seamounts at various stages of subduction. We also observe changes in Moho depth that we attribute to offsets on the Alvin Canyon Fault and changes in the density of the overriding plate. We hypothesize that seamounts G2 and M2 are responsible for the two clusters of seismicity in this region. Additionally, the trajectories of several potential seamounts correlate with slides and scars in the deformation front and broad regions of uplift on the continental shelf. Here, we see evidence of the long-term deformation caused by these features and evidence suggesting that two of these features are actively fracturing the overriding plate, resulting in observable seismicity.

We propose that changes in velocity structure and Moho depth contribute to a complex forearc structure and a megathrust segment boundary near 44.5°N. The combination of subducting seamounts and changes in slab depth along-strike contributes to a rough subduction interface. Rugged plate interfaces are observed to correlate with smaller megathrust earthquakes and lower coupling compared to smooth plate boundaries. Rugged megathrusts are also associated with rupture barriers and aseismic creeping. One way in which these features may be responsible for the low coupling ratio observed in this region is by changing pore pressure around the top of the crust. Our observations provide a holistic view of the interplay between surface and subducting structures and the resulting seismic behavior along the central Oregon margin.

Acknowledgments

We extend our sincere thanks to the volunteers who helped deploy and recover the seismic nodes for the Cascadia2021 project. We acknowledge that this work would not have been possible without the landowners and land managers who allowed us to deploy these instruments on their land. The deployment of the land-based stations as part of the Cascadia2021 experiment, as well as support for the graduate research student, was funded by NSF grants EAR-1946426, EAR-1946347, and EAR-1946396. Nodal instruments were provided by EarthScope Primary Instrument Center. We thank Pablo Canales and Suzanne Carbotte for leading the 2021 research cruises during which the ocean-bottom seismometers and airgun sources were deployed. The legacy data was funded by NSF grants OCE-8900962, EAR-8905189 (for the 1989 experiment), and EAR-1147975 (2012), as well as USGS grants 14-08-0001-G2072 (1989) and 1434HQ-96GR0725 (1996). Special thanks to Kathy Davenport for her assistance with permitting the 2021 sites, and to both Chris Kenyon and Kathy Davenport for their efforts in processing the 2012 data. This work benefited from access to the University of Oregon's high-performance computing cluster, Talapas. Any mention of trade, firm, or product names is for descriptive purposes only and does not imply endorsement by the U.S. Government. Lastly, we would like to thank Suzanne Carbotte and Dan Bassett, whose reviews helped significantly improve this work. We also thank our USGS reviewers Fred Pollitz and John Tinsley for providing thoughtful and constructive reviews.

Data and code availability

The 2021 seismic data are all publicly available. The seismic data acquired through the Cascadia2021 experiment are available in PH5 format under network code Z4 2021 in the online repository of the Seismological Facility for the Advancement of Geoscience (SAGE), which is operated by the Earthscope Consortium (https://ds.iris.edu/gmap/#network=Z4&starttime=2021-04-01&endtime=2021-08-01&maxlat=49&maxlon=-121&minlat=41&minlon=-125&drawingmode=box&planet=earth). The 2021 OBS data (Canales et al., 2023) can be accessed through network code YR 2021, doi:10.7914/SN/YR_2021 (https://ds.iris.edu/gmap/#network=YR&starttime=2021-04-01&endtime=2021-08-01&maxlat=48&maxlon=-121&minlat=42&minlon=-126&drawingmode=box&planet=earth). The seismic shot information for the CASIE21 experiment is available through the Marine Geoscience Data System (MGDS) repository doi:10.26022/IEDA/330905 (Carbotte et al., 2024).

Competing interests

The authors declare that they have no competing interests.

References

Allam, A. A. and Ben-Zion, Y. Seismic velocity structures in the southern California plate-boundary environment from double-difference tomography. *Geophysical Journal International*, 190 (2), 2012. doi: 10.1111/j.1365-246x.2012.05544.x.

Arai, R., Kodaira, S., Henrys, S., Bangs, N., Obana, K., Fujie, G., Miura1, S., Barker, D., Bassett, D., Bell, R., Mochizuki, K., Kellett, R., Stucker, V., Fry, B., and Team, N. Three-dimensional P wave

velocity structure of the northern Hikurangi margin from the NZ3D experiment: Evidence for fault-bound anisotropy. *Journal of Geophysical Research: Solid Earth*, 125(12), Nov. 2020. doi: 10.1029/2020jb020433.

Arnulf, A. F., Bassett, D., Harding, A. J., Kodaira, S., Nakanishi, A., and Moore, G. Upper-plate controls on subduction zone geometry, hydration and earthquake behaviour. *Nature Geoscience*, 15(2):143–148, Feb. 2022. doi: 10.1038/s41561-021-00879-x.

Ashraf, A. and Hooft, E. E. E. Shoreline crossing Moho geometry of the Cascadia slab: CascadiaMoho1.0. *Seismica*, 2(4), Feb. 2026. doi: 10.26443/seismica.v2i4.1674.

Ashraf, A., Hooft, E. E. E., Toomey, D. R., Tréhu, A. M., Nolan, S., Wirth, E. A., and Ward, K. M. A High-Resolution 3-D P-Wave Velocity Structure of the South-Central Cascadia Subduction Zone From Wide-Angle Shore-Crossing Seismic Refraction Data. *Journal of Geophysical Research: Solid Earth*, 130(2), Feb. 2025. doi: 10.1029/2024jb029525.

Babendreier, C. M. *Seismic investigation of massive submarine landslide deposits offshore Oregon and subducting North American plate along the Puerto Rico Trench*. PhD thesis, University of Texas at Austin, 2023. https://repositories.lib.utexas.edu/items/81ef94ce-9555-4a66-8859-211557034b00.

Bassett, D. and Watts, A. B. Gravity anomalies, crustal structure, and seismicity at subduction zones: 1. Seafloor roughness and subducting relief. *Geochemistry, Geophysics, Geosystems*, 16(5): 1508–1540, Mar. 2015. doi: 10.1002/2014gc005684.

Bassett, D., Shillington, D. J., Wallace, L. M., and Elliott, J. L. Variation in slip behaviour along megathrusts controlled by multiple physical properties. *Nature Geoscience*, 18(1):20–31, Jan. 2025. doi: 10.1038/s41561-024-01617-9.

Bloch, W., Bostock, M. G., and Audet, P. A Cascadia Slab Model From Receiver Functions. *Geochemistry, Geophysics, Geosystems*, 24(10), Oct. 2023. doi: 10.1029/2023gc011088.

Bodmer, M., Toomey, D. R., Hooft, E. E. E., and Schmandt, B. Buoyant Asthenosphere Beneath Cascadia Influences Megathrust Segmentation. *Geophysical Research Letters*, 45(14), 2018. doi: 10.1029/2018gl078700.

Bodmer, M., Toomey, D. R., VanderBeek, B., Hooft, E. E., and Byrnes, J. S. Body Wave Tomography of the Cascadia Subduction Zone and Juan de Fuca Plate System: Identifying Challenges and Solutions for Shore-Crossing Data. *Geochemistry, Geophysics, Geosystems*, 21(12), Dec. 2020. doi: 10.1029/2020gc009316.

Brudzinski, M. R. and Allen, R. M. Segmentation in episodic tremor and slip all along Cascadia. *Geology*, 35(10):907, 2007. doi: 10.1130/g23740a.1.

Bécel, A., Shillington, D. J., Delescluse, M., Nedimović, M. R., Abers, G., Saffer, D. M., Webb, S. C., Keranen, K. M., Roche, P.-H., Li, J., and Kuehn, H. Tsunamigenic structures in a creeping section of the Alaska subduction zone. *Nature Geoscience*, 10(8), 2017. doi: 10.1038/ngeo2990.

Canales, J. P., Carbotte, S. M., Nedimović, M. R., and Carton, H. Dry Juan de Fuca slab revealed by quantification of water entering Cascadia subduction zone. *Nature Geoscience*, 10(11):864–870, Oct. 2017. doi: 10.1038/ngeo3050.

Canales, J. P., Miller, N. C., Baldwin, W., Carbotte, S. M., Han, S., Boston, B., Jian, H., Collins, J., and Lizarralde, D. CASIE21-OBS: An Open-Access, OBS Controlled-Source Seismic Data Set for Investigating the Structure and Properties of the Cascadia Accretionary Wedge and the Downgoing Explorer-Juan de Fuca-Gorda Plate System. *Seismological Research Letters*, May 2023. doi: 10.1785/0220230010.

Carbotte, S. M., Boston, B., Han, S., Shuck, B., Canales, J. P., Beeson, J. W., Nedimovic, M. R., and Tobin, H. J. New Observations of Plate Interface Depth and Geometry at the Offshore Cascadia Subduction Zone from the CAscadia Seismic Imaging Experiment 2021 (CASIE21) and Comparisons with Existing Plate Depth Models. In *Fall Meeting 2022*. AGU, 2022.

Carbotte, S. M., Boston, B., Han, S., Shuck, B., Beeson, J., Canales, J. P., Tobin, H., Miller, N., Nedimovic, M., Tréhu, A., Lee, M., Lucas, M. C., Jian, H., Jiang, D., Moser, L., Anderson, C., Judd, D., Fernandez, J., Campbell, C., Goswami, A., and Gahlawat, R. Subducting plate structure and megathrust morphology from deep seismic imaging linked to earthquake rupture segmentation at Cascadia. *Science Advances*, 10(23), 2024. doi: 10.1126/sciadv.adl3198.

Chesley, C., Naif, S., Key, K., and Bassett, D. Fluid-rich subducting topography generates anomalous forearc porosity. *Nature*, 595 (7866), 2021. doi: 10.1038/s41586-021-03619-8.

Delph, J. R., Thomas, A. M., and Levander, A. Subcretionary tectonics: Linking variability in the expression of subduction along the Cascadia forearc. *Earth and Planetary Science Letters*, 556: 116724, Feb. 2021. doi: 10.1016/j.epsl.2020.116724.

DeMets, C., Gordon, R. G., and Argus, D. F. Geologically current plate motions. *Geophysical Journal International*, 181(1):1–80, Apr. 2010. doi: 10.1111/j.1365-246x.2009.04491.x.

Dominguez, S., Lallemand, S., Malavieille, J., and von Huene, R. Upper plate deformation associated with seamount subduction. *Tectonophysics*, 293(3-4):207–224, Aug. 1998. doi: 10.1016/s0040-1951(98)00086-9.

Dunham, A. and Kiser, E. Local earthquake tomography of the Central Oregon forearc using a large-N, short duration, nodal array. *Earth and Planetary Science Letters*, 551:116559, Dec. 2020. doi: 10.1016/j.epsl.2020.116559.

Dunn, R. A., Lekić, V., Detrick, R. S., and Toomey, D. R. Three-dimensional seismic structure of the Mid-Atlantic Ridge (35°N): Evidence for focused melt supply and lower crustal dike injection. *Journal of Geophysical Research: Solid Earth*, 110(B9), 2005. doi: 10.1029/2004jb003473.

Egbert, G. D., Yang, B., Bedrosian, P. A., Key, K., Livelybrooks, D. W., Schultz, A., Kelbert, A., and Parris, B. Fluid transport and storage in the Cascadia forearc influenced by overriding plate lithology. *Nature Geoscience*, 15(8), 2022. doi: 10.1038/s41561-022-00981-8.

Fleming, S. W. and Tréhu, A. M. Crustal structure beneath the central Oregon convergent margin from potential-field modeling: Evidence for a buried basement ridge in local contact with a seaward dipping backstop. *Journal of Geophysical Research: Solid Earth*, 104(B9), 1999. doi: 10.1029/1999jb900159.

Gase, A. C., Van Avendonk, H. J. A., Bangs, N. L., Bassett, D., Henrys, S. A., Barker, D. H. N., Kodaira, S., Jacobs, K. M., Luckie, T. W., Okaya, D. A., Fujie, G., Yamamoto, Y., Arnulf, A. F., and Arai, R. Crustal Structure of the Northern Hikurangi Margin, New Zealand: Variable Accretion and Overthrusting Plate Strength Influenced by Rough Subduction. *Journal of Geophysical Research: Solid Earth*, 126(5), May 2021. doi: 10.1029/2020jb021176.

Gerdom, M., Tréhu, A., Flueh, E., and Klaeschen, D. The continental margin off Oregon from seismic investigations. *Tectonophysics*, 329(1-4):79–97, Dec. 2000. doi: 10.1016/s0040-1951(00)00190-6.

Goldfinger, C., Kulm, L. D., Yeats, R. S., McNeill, L., and Hummon, C. Oblique strike-slip faulting of the central Cascadia submarine forearc. *Journal of Geophysical Research: Solid Earth*, 102(B4): 8217–8243, Apr. 1997. doi: 10.1029/96jb02655.

Goldfinger, C., Nelson, C. H., Morey, A. E., Johnson, J. E., Patton, J. R., Karabanov, E. B., Gutierrez-Pastor, J., Eriksson, A. T., Gracia, E., Dunhill, G., Enkin, R. J., Dallimore, A., and Vallier, T. Tur-

bidite Event History—Methods and Implications for Holocene Paleoseismicity of the Cascadia Subduction Zone. Technical report, US Geological Survey, 2012.

Han, S., Carbotte, S. M., Canales, J. P., Nedimović, M. R., Carton, H., Gibson, J. C., and Horning, G. W. Seismic reflection imaging of the Juan de Fuca plate from ridge to trench: New constraints on the distribution of faulting and evolution of the crust prior to subduction. *Journal of Geophysical Research: Solid Earth*, 121 (3):1849–1872, Mar. 2016. doi: 10.1002/2015jb012416.

Hole, J. A., Catchings, R. D., Clair, K. C. S., Rymer, M. J., Okaya, D. A., and Carney, B. J. Steep-Dip Seismic Imaging of the Shallow San Andreas Fault Near Parkfield. *Science*, 294(5546):1513–1515, Nov. 2001. doi: 10.1126/science.1065100.

Horning, G., Canales, J. P., Carbotte, S. M., Han, S., Carton, H., Nedimović, M. R., and van Keken, P. E. A 2-D tomographic model of the Juan de Fuca plate from accretion at axial seamount to subduction at the Cascadia margin from an active source ocean bottom seismometer survey. *Journal of Geophysical Research: Solid Earth*, 121(8):5859–5879, Aug. 2016. doi: 10.1002/2016jb013228.

Kenyon, C. A 3-D Tomographic Model of the P-wave Velocity Structure of the Central Cascadia Forearc. Master's thesis, Oregon State University, Mar. 2016.

Kenyon, C., Tréhu, A. M., Toomey, D. R., Wilcock, W. S., Carbotte, S. M., Carton, H. D., and Canales, J. A 3D velocity model of the central Cascadia subduction zone beneath the Oregon continental shelf and Coast Range. In *AGU Fall Meeting Abstracts*, volume 2013, pages S21C–2446, 2013.

Kopp, H. Invited review paper: The control of subduction zone structural complexity and geometry on margin segmentation and seismicity. *Tectonophysics*, 589:1–16, Mar. 2013. doi: 10.1016/j.tecto.2012.12.037.

Leonard, L. J., Currie, C. A., Mazzotti, S., and Hyndman, R. D. Rupture area and displacement of past Cascadia great earthquakes from coastal coseismic subsidence. *Geological Society of America Bulletin*, 122(11-12), 2010. doi: 10.1130/b30108.1.

Li, S., Wang, K., Wang, Y., Jiang, Y., and Dosso, S. E. Geodetically Inferred Locking State of the Cascadia Megathrust Based on a Viscoelastic Earth Model. *Journal of Geophysical Research: Solid Earth*, 123(9), 2018. doi: 10.1029/2018jb015620.

Lindsey, E. O., Mallick, R., Hubbard, J. A., Bradley, K. E., Almeida, R. V., Moore, J. D. P., Bürgmann, R., and Hill, E. M. Slip rate deficit and earthquake potential on shallow megathrusts. *Nature Geoscience*, 14(5):321–326, May 2021. doi: 10.1038/s41561-021-00736-x.

Martínez-Loriente, S., Sallarès, V., R. Ranero, C., B. Ruh, J., Barckhausen, U., Grevemeyer, I., and Bangs, N. Influence of Incoming Plate Relief on Overriding Plate Deformation and Earthquake Nucleation: Cocos Ridge Subduction (Costa Rica). *Tectonics*, 38 (12):4360–4377, Dec. 2019. doi: 10.1029/2019tc005586.

Maus, S. EMAG2: Earth Magnetic Anomaly Grid (2-arc-minute resolution), 2009. https://www.ncei.noaa.gov/access/metadata/landing-page/bin/iso?id=gov.noaa.ngdc.mgg.geophysical_models:EMAG2. doi: 10.7289/V5MW2F2P.

McCaffrey, R., Qamar, A. I., King, R. W., Wells, R., Khazaradze, G., Williams, C. A., Stevens, C. W., Vollick, J. J., and Zwick, P. C. Fault locking, block rotation and crustal deformation in the Pacific Northwest. *Geophysical Journal International*, 169(3), 2007. doi: 10.1111/j.1365-246x.2007.03371.x.

McLaughlin, R. J., Sliter, W. V., Frederiksen, N. O., Harbert, W. P., and McCulloch, D. S. Plate motions recorded in tectonostratigraphic terranes of the Franciscan complex and evolution of the Mendocino triple junction, northwestern California. Technical report, USGS, 1997.

McNeill, L. C., Goldfinger, C., Kulm, L. D., and Yeats, R. S. Tectonics of the Neogene Cascadia forearc basin: Investigations of a deformed late Miocene unconformity. *Geological Society of America Bulletin*, 112(8):1209–1224, Aug. 2000. doi: 10.1130/0016-7606(2000)112<1209:totncf>2.0.co;2.

Melgar, D. Was the January 26th, 1700 Cascadia Earthquake Part of a Rupture Sequence? *Journal of Geophysical Research: Solid Earth*, 126(10), Oct. 2021. doi: 10.1029/2021jb021822.

Monigle, P. W., Bohnenstiehl, D. R., Tolstoy, M., and Waldhauser, F. Seismic tremor at the 9°50'N East Pacific Rise eruption site. *Geochemistry, Geophysics, Geosystems*, 10(11), Nov. 2009. doi: 10.1029/2009gc002561.

Morton, E. A., Bilek, S. L., and Rowe, C. A. Newly detected earthquakes in the Cascadia subduction zone linked to seamount subduction and deformed upper plate. *Geology*, 46(11), 2018. doi: 10.1130/g45354.1.

Morton, E. A., Bilek, S. L., and Rowe, C. A. Cascadia Subduction Zone Fault Heterogeneities From Newly Detected Small Magnitude Earthquakes. *Journal of Geophysical Research: Solid Earth*, 128(6), May 2023. doi: 10.1029/2023jb026607.

Moser, T. J. Shortest path calculation of seismic rays. *Geophysics*, 56(1):59–67, Jan. 1991. doi: 10.1190/1.1442958.

Philip, B. T., Solomon, E. A., Kelley, D. S., Tréhu, A. M., Whorley, T. L., Roland, E., Tominaga, M., and Collier, R. W. Fluid sources and overpressures within the central Cascadia Subduction Zone revealed by a warm, high-flux seafloor seep. *Science Advances*, 9 (4), Jan. 2023. doi: 10.1126/sciadv.add6688.

Ryan, W. B. F., Carbotte, S. M., Coplan, J. O., O'Hara, S., Melkonian, A., Arko, R., Weissel, R. A., Ferrini, V., Goodwillie, A., Nitsche, F., Bonczkowski, J., and Zemsky, R. Global Multi-Resolution Topography synthesis. *Geochemistry, Geophysics, Geosystems*, 10 (3), Mar. 2009. doi: 10.1029/2008gc002332.

Saffer, D. M. Mapping fluids to subduction megathrust locking and slip behavior. *Geophysical Research Letters*, 44(18), 2017. doi: 10.1002/2017gl075381.

Sandwell, D. T., Müller, R. D., Smith, W. H. F., Garcia, E., and Francis, R. New global marine gravity model from CryoSat-2 and Jason-1 reveals buried tectonic structure. *Science*, 346(6205):65–67, Oct. 2014. doi: 10.1126/science.1258213.

Satake, K., Wang, K., and Atwater, B. F. Fault slip and seismic moment of the 1700 Cascadia earthquake inferred from Japanese tsunami descriptions. *Journal of Geophysical Research: Solid Earth*, 108(B11), Nov. 2003. doi: 10.1029/2003jb002521.

Schmalzle, G. M., McCaffrey, R., and Creager, K. C. Central Cascadia subduction zone creep. *Geochemistry, Geophysics, Geosystems*, 15(4):1515–1532, Apr. 2014. doi: 10.1002/2013gc005172.

Segovia, M., Font, Y., Régnier, M., Charvis, P., Galve, A., Nocquet, J., Jarrín, P., Hello, Y., Ruiz, M., and Pazmiño, A. Seismicity Distribution Near a Subducting Seamount in the Central Ecuadorian Subduction Zone, Space-Time Relation to a Slow-Slip Event. *Tectonics*, 37(7), 2018. doi: 10.1029/2017tc004771.

Shaddox, H. R. and Schwartz, S. Y. Subducted seamount diverts shallow slow slip to the forearc of the northern Hikurangi subduction zone, New Zealand. *Geology*, 47(5):415–418, Mar. 2019. doi: 10.1130/g45810.1.

Shaw, P. R. and Orcutt, J. A. Waveform inversion of seismic refraction data and applications to young Pacific crust. *Geophysical Journal International*, 82(3), 1985. doi: 10.1111/j.1365-246x.1985.tb05143.x.

Shillington, D. J., Bécel, A., Nedimović, M. R., Kuehn, H., Webb, S. C., Abers, G. A., Keranen, K. M., Li, J., Delescluse, M., and Mattei-Salicrup, G. A. Link between plate fabric, hydration and subduction zone seismicity in Alaska. *Nature Geoscience*, 8(12):

961–964, Nov. 2015. doi: 10.1038/ngeo2586.

Stone, I., Vidale, J. E., Han, S., and Roland, E. Catalog of Offshore Seismicity in Cascadia: Insights Into the Regional Distribution of Microseismicity and its Relation to Subduction Processes. *Journal of Geophysical Research: Solid Earth*, 123(1):641–652, Jan. 2018. doi: 10.1002/2017jb014966.

Todd, E. K., Schwartz, S. Y., Mochizuki, K., Wallace, L. M., Sheehan, A. F., and Webb, S. C. Earthquakes and Tremor Linked to Seamount Subduction During Shallow Slow Slip at the Hikurangi Margin, New Zealand. *Journal of Geophysical Research: Solid Earth*, 123(8):6769–6783, Aug. 2018. doi: 10.1029/2018jb016136.

Toomey, D. R. and Foulger, G. R. Tomographic inversion of local earthquake data from the Hengill-Grensdalur Central Volcano Complex, Iceland. *Journal of Geophysical Research: Solid Earth*, 94(B12):17497–17510, Dec. 1989. doi: 10.1029/jb094ib12p17497.

Toomey, D. R., Solomon, S. C., and Purdy, G. M. Tomographic imaging of the shallow crustal structure of the East Pacific Rise at 9°30'N. *Journal of Geophysical Research: Solid Earth*, 99(B12): 24135–24157, Dec. 1994. doi: 10.1029/94jb01942.

Torres, M. E., Embley, R. W., Merle, S. G., Tréhu, A. M., Collier, R. W., and Suess, E. andHeeschen, K. U. Methane sources feeding cold seeps on the shelf and upper continental slope off central Oregon, USA. *Geochemistry, Geophysics, Geosystems*, 10(11), Nov. 2009. doi: 10.1029/2009gc002518.

Tréhu, A., Wilcock, W., Hilmo, R., Bodin, P., Connelly, J., Roland, E., and Braunmiller, J. The Role of the Ocean Observatories Initiative in Monitoring the Offshore Earthquake Activity of the Cascadia Subduction Zone. *Oceanography*, 31(1):104–113, Mar. 2018. doi: 10.5670/oceanog.2018.116.

Tréhu, A., Hooft, E. E., Ward, K. M., Wirth, E., and Stone, I. Field report for the Cascadia2021 Seismic Node Experiment. Field Report, Oregon State University, Mar. 2022a. https://blogs.oregonstate.edu/cascadia2021/2022/06/08/field-data-report/.

Tréhu, A. M., Asudeh, I., Brocher, T. M., Luetgert, J. H., Mooney, W. D., Nabelek, J. L., and Nakamura, Y. Crustal Architecture of the Cascadia Forearc. *Science*, 266(5183):237–243, Oct. 1994. doi: 10.1126/science.266.5183.237.

Tréhu, A. M., Braunmiller, J., and Nabelek, J. L. Probable low-angle thrust earthquakes on the Juan de Fuca–North America plate boundary. *Geology*, 36(2):127, 2008. doi: 10.1130/g24145a.1.

Tréhu, A. M., Blakely, R. J., and Williams, M. C. Subducted seamounts and recent earthquakes beneath the central Cascadia forearc. *Geology*, 40(2):103–106, Feb. 2012. doi: 10.1130/g32460.1.

Tréhu, A. M., Braunmiller, J., and Davis, E. Seismicity of the Central Cascadia Continental Margin near 44.5 N: A Decadal View. *Seismological Research Letters*, 86(3):819–829, Apr. 2015. doi: 10.1785/0220140207.

Tréhu, A. M., Tominaga, M., Lyle, M., Davenport, K., Phrampus, B. J., Favorito, J., Zhang, E., Lenz, B. L., Shreedharan, S., Yelisetti, S., and Party, T. R. S. The Hidden History of the South-Central Cascadia Subduction Zone Recorded on the Juan de Fuca Plate Offshore Southwest Oregon. *Geochemistry, Geophysics, Geosystems*, 23(9), 2022b. doi: 10.1029/2021gc010318.

Tréhu, A. M., Davenport, K., Kenyon, C. B., Carbotte, S. M., Nabelek, J. L., Toomey, D. R., and Wilcock, W. S. D. Deformation of the Juan de Fuca Plate Beneath the Central Cascadia Continental Margin (44°-45°N) in Response to an Upper Plate Load. *Earth Science, Systems and Society*, 3(1), Nov. 2023. doi: 10.3389/esss.2023.10085.

von Huene, R., Ranero, C. R., Weinrebe, W., and Hinz, K. Quaternary convergent margin tectonics of Costa Rica, segmentation of the Cocos Plate, and Central American volcanism. *Tectonics*, 19(2): 314–334, Apr. 2000. doi: 10.1029/1999tc001143.

Walton, M. A., Staisch, L. M., Dura, T., Pearl, J. K., Sherrod, B., Gomberg, J., Engelhart, S., Tréhu, A., Watt, J., Perkins, J., Witter, R. C., Bartlow, N., Goldfinger, C., Kelsey, H., Morey, A. E., Sahakian, V. J., Tobin, H., Wang, K., Wells, R., and Wirth, E. Toward an Integrative Geological and Geophysical View of Cascadia Subduction Zone Earthquakes. *Annual Review of Earth and Planetary Sciences*, 49(1):367–398, May 2021. doi: 10.1146/annurev-earth-071620-065605.

Wang, K. and Bilek, S. L. Invited review paper: Fault creep caused by subduction of rough seafloor relief. *Tectonophysics*, 610: 1–24, Jan. 2014. doi: 10.1016/j.tecto.2013.11.024.

Wang, K. and Tréhu, A. M. Invited review paper: Some outstanding issues in the study of great megathrust earthquakes—The Cascadia example. *Journal of Geodynamics*, 98:1–18, Aug. 2016. doi: 10.1016/j.jog.2016.03.010.

Wang, P., Engelhart, S. E., Wang, K., Hawkes, A. D., Horton, B. P., Nelson, A. R., and Witter, R. C. Heterogeneous rupture in the great Cascadia earthquake of 1700 inferred from coastal subsidence estimates. *Journal of Geophysical Research: Solid Earth*, 118(5):2460–2473, May 2013. doi: 10.1002/jgrb.50101.

Wang, Y., Lin, F.-C., and Ward, K. M. Ambient noise tomography across the Cascadia subduction zone using dense linear seismic arrays and double beamforming. *Geophysical Journal International*, 217(3):1668–1680, Feb. 2019. doi: 10.1093/gji/ggz109.

Watt, J. T. and Brothers, D. S. Systematic characterization of morphotectonic variability along the Cascadia convergent margin: Implications for shallow megathrust behavior and tsunami hazards. *Geosphere*, 17(1):95–117, Nov. 2020. doi: 10.1130/ges02178.1.

Wech, A. G. Cataloging Tectonic Tremor Energy Radiation in the Cascadia Subduction Zone. *Journal of Geophysical Research: Solid Earth*, 126(10), Oct. 2021. doi: 10.1029/2021jb022523.

Wells, R., Bukry, D., Friedman, R., Pyle, D., Duncan, R., Haeussler, P., and Wooden, J. Geologic history of Siletzia, a large igneous province in the Oregon and Washington Coast Range: Correlation to the geomagnetic polarity time scale and implications for a long-lived Yellowstone hotspot. *Geosphere*, 10(4):692–719, Aug. 2014. doi: 10.1130/ges01018.1.

Williams, M. C., Tréhu, A. M., and Braunmiller, J. Seismicity at the Cascadia Plate Boundary beneath the Oregon Continental Shelf. *Bulletin of the Seismological Society of America*, 101(3):940–950, May 2011. doi: 10.1785/0120100198.

Wilson, D. S. The Juan de Fuca plate and slab: isochron structure and Cenozoic plate motions. Technical report, Natural Resources Canada/CMSS/Information Management, 2002.

Yeats, R. S., Kulm, L. D., Goldfinger, C., and McNeill, L. C. Stonewall anticline: An active fold on the Oregon continental shelf. *Geological Society of America Bulletin*, 110(5):572–587, May 1998. doi: 10.1130/0016-7606(1998)110<0572:saaafo>2.3.co;2.

The article *Subducted Structure in Central Cascadia from Margin-Crossing Seismic Tomography* © 2026 by Sarah Nolan is licensed under CC BY 4.0.